University of Groningen

Mechanisms in iron, nickel, and manganese, catalysis with small molecule oxidants
Padamati, Sandeep

Link to publication in University of Groningen/UMCG research database

Chapter 5
Transient Formation and Reactivity of a High Valent Nickel(IV) Oxido Complex

Abstract

A reactive high valent dinuclear nickel(IV) oxido bridged complex is reported that can be formed at room temperature by reaction of $[(L)_2Ni(II)_2(\mu\text{-}X)_3]X$ (X = Cl or Br) with NaOCl in methanol or acetonitrile (where L = 1,4,7-trimethyl-1,4,7-triazacyclononane). The unusual Ni(IV) oxido species is stabilized within a dinuclear tris-μ-oxido bridged structure as $[(L)_2Ni(IV)_2(\mu\text{-}O)_3]^{2+}$. Its structure and its reactivity with organic substrates is demonstrated through a combination of UV-vis absorption, resonance Raman, ^{1}H NMR, and EPR spectroscopy, ESI mass spectrometry, and DFT methods. The identification of a Ni(IV)-O species opens opportunities to control the reactivity of NaOCl for selective oxidations.
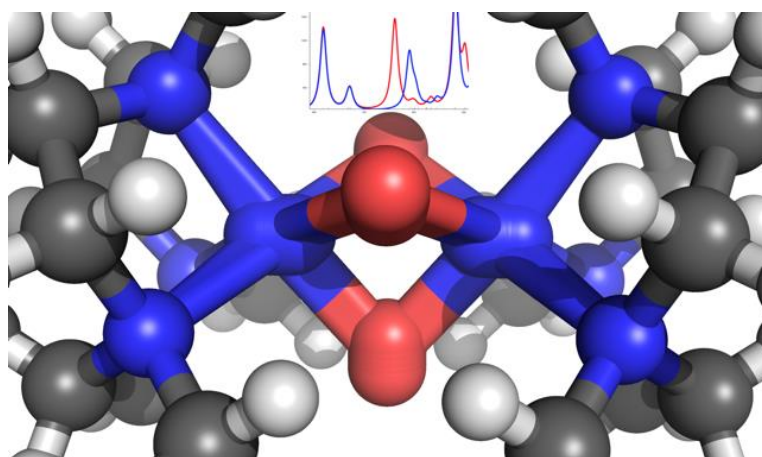
S K. Padamati, D Angelone, A Draksharapu, G Primi, M. Swart, W R. Browne, to be submitted.

5.1 Introduction

Metalloenzymes are central to the functioning of biological systems, especially in oxidative transformations and protection against reactive oxygen species.[1] Fe, Cu, and Mn dependent metalloenzymes have been studied extensively, and have stimulated the design and synthesis of structural and functional model complexes, especially, in the search for synthetic analogues of reactive bioinorganic intermediates.[2] Recently, attention has turned to synthetic nickel based complexes due to enzymes such as NOD (nickel oxide dismutase),[3] and their potential in the activation of small molecules, including H_2O_2,[4] mCPBA[5] and NaOCl.[6] In the latter case, such complexes open the possibility to achieve selective alkane chlorination, and alkane and alkene oxygenation.

Recently, several high valent (Ni(III)[4,7] and Ni(IV)[6(c),8]) intermediates were identified spectroscopically. In contrast to organometallic Ni(IV) complexes,[8] the formation of Ni(III) and, more so, Ni(IV) oxido complexes, although inferred, is controversial due to the implications of the oxo-wall premise.[9] Nevertheless, several Ni(II) and Ni(III) oxido or peroxido complexes, formed with O_2 and H_2O_2 have been characterized already at low temperature.[19,20,21,22]

Here we show that a novel room temperature stable dinuclear Ni(IV) oxido complex (**3**) $[(L)_2Ni(IV)_2(\mu\text{-}O)_3]^{2+}$ (where L = 1,4,7-trimethyl-1,4,7-triazacyclononane) can be generated by reaction of the Ni(II) complexes (**1**, **2**) with NaOCl (Scheme 1). The high oxidation state of **3** is stabilized by the tris-μ-oxido bridged dinuclear structure. Furthermore, the reactivity of **3** towards direct C-H oxidation of organic substrates is demonstrated.

Complex **3** is obtained within seconds of addition of near stoichiometric amounts of NaOCl to $[(L)_2Ni(II)_2(\mu\text{-}X)_3]X\cdot(H_2O)_n$ (where X = Cl (**1**) or Br (**2**), n = 5 or 8)[10] in methanol or acetonitrile at room temperature. The structure of **3** was elucidated through a combination of UV-vis absorption and resonance Raman spectroscopy and ESI mass spectrometry, supported by isotope labelling, cross-over experiments and DFT methods.
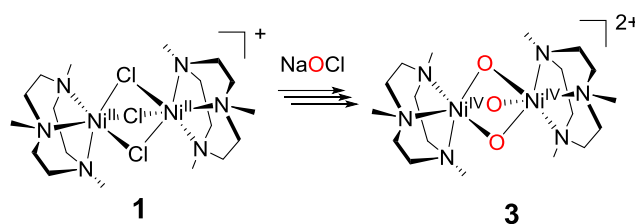
Scheme 1 Formation of **3** from **1** and NaOCl

5.2 Results and discussion

Complexes **1** and **2** were prepared by methods analogous to those reported earlier.[10] The Raman spectra of **1** in the solid state (Figure S1) and in solution (i.e. methanol, acetonitrile, Figure S2) indicate that the complexes retain their structure, i.e. the ligand (L) remains bound to Ni(II) upon dissolution. However, ESI mass spectrometry indicates that **1** can form mononuclear complexes with three (176.3 m/z: **4** $[(L)Ni(II)(CH_3CN)_3)]^{2+}$) or two acetonitrile ligands (155.9 m/z: **5**, $([(L)Ni(II)(CH_3CN)_2)]^{2+}$) by substitution of the chlorido ligands (Figure S3). Indeed, mixtures of **1** and **2** show rapid exchange of Cl^- and Br^- ligands (Figure S4). The ^1H NMR spectrum of **1** in acetonitrile shows paramagnetically shifted and broadened signals at ca. 60, 90, and 120 ppm (Figure S5) and its UV-vis

absorption spectrum in methanol and acetonitrile (Figure S6) show bands at 322, 541 and 884 nm. The DFT data (vide infra) indicate anti-ferromagnetically coupled Ni(II) ions in **1** and **2**, in agreement with observations by Wieghardt et al.[11] The C_{3h}-symmetric structure for both **1** and **2** corresponds to the X-ray structure, with differences of ca. 0.01-0.02 Å for Ni-Cl/Br and Ni-Ni distances (Table S1). The anti-ferromagnetically coupled (open-shell singlet) state lies lowest in energy,[12,13] albeit only 0.3 kcal·mol^{-1} lower than the ferromagnetically coupled (S=2) state, with other spin states (S=1, S=0) higher in energy by >23 kcal·mol^{-1} (incl. COSMO solvation[14] and ZORA[15] relativistic effects, Table S2). The NMR and UV-vis absorption spectra are similar to those of related Ni(II) complexes (Figure S7).[16]

Addition of NaOCl to **1** or **2** in methanol or in acetonitrile leads to a rapid increase in absorbance at 363 nm and 612 nm due to formation of **3** (Figure 1). In methanol, the visible absorption band decreases with $t_{1/2}$ of ca. 50 s at 20 °C (Figure S8) and the absorption spectrum after 20 min is similar to the initial spectrum, with only a minor shift from 388 nm to 378 nm (Figure 1). Notably, the rate of decay of **3** in methanol was substantially lower than the rate of the direct reaction of NaOCl with methanol in the absence of **1** (Figure S8) indicating that the formation of **3** competes with oxidation of methanol by NaOCl, and that **3** is less reactive in the oxidation of methanol than NaOCl.
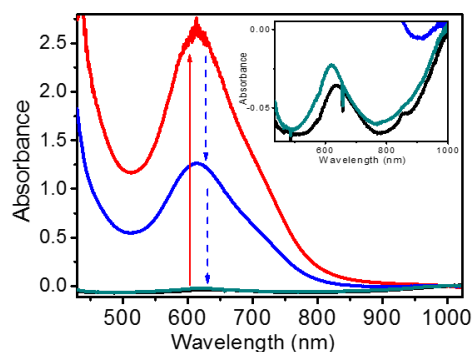

Figure 1 UV-vis absorption spectrum of **1** (3.5 mM) in methanol before (black) and after (red 6 s, blue 48 s, green 463 s) addition of 11 equiv. NaOCl(aq) at 293 K. Inset: expansion of NIR region. The data indicate that for **3** $\lambda_{612\ nm}$ > 715 M^{-1} cm^{-1}.

In both the presence and absence of **1**, near quantitative (w.r.t. NaOCl) oxidation of methanol to formaldehyde occurs (1.5:1, Figure S9), indicating that although at least 2 equiv. of NaOCl are consumed in forming **3** from **1**, these oxidation equivalents are still available for subsequent oxidation of methanol. Further additions of NaOCl in the presence of **1** resulted in the reappearance of the 612 nm absorption (Figure S10), confirming the integrity of the catalyst under reaction conditions. Similar changes were observed with NaOBr (Figure S10c and S11), which indicates that the same intermediate is formed with both oxidants (vide infra). Addition of H_2O_2 or purging with O_2 (Figure S12 and S13) did not result in the appearance of **3**.

Intermediate **3** forms upon addition of NaOCl to **1** also in acetonitrile (absorbance band at 612 nm), but persists for a substantially longer time period than in methanol, with $t_{1/2}$ of ca. 10 min at 20 °C and over 6 h at -15 °C, (Figures S14 and S15), enabling characterization by resonance Raman spectroscopy and ESI mass spectrometry and reactivity with other substrates to be studied (vide infra). The maximum transient

absorbance at 612 nm was obtained with 3-4 equiv. of NaOCl (Figure S16). The three broad signals in the ^{1}H NMR spectrum of **1** in acetonitrile decrease upon addition of NaOCl and then recover concomitant with the increase and decrease in absorbance at 612 nm (Figure S17). Samples flash frozen to 77 K at any time, however, did not indicate the presence of a mononuclear Ni(III) species by X-band EPR spectroscopy. Notably, addition of NaOCl to **4** in acetonitrile results in the same visible absorption spectrum as obtained with **1** (Figure S18) indicating that the formation of **3** is not dependent on the initial form of the LNi(II) complex (with Cl$^-$/Br$^-$/CH$_3$CN) and is consistent with the rapid equilibration of these species in solution. Furthermore, addition of NaOCl (4.5-11 equiv.) to a 1:1 mixture of NiCl$_2$ and the ligand (L) in acetonitrile results in the appearance of the bands at λ_{max} 363 nm and 612 nm (Figure S19), consistent with a max. 50% conversion to **3**. In the absence of ligand (i.e. only NiCl$_2\cdot$6H$_2$O) the band at 612 nm was not observed (Figure S20).

In earlier reports,[6] the presence of acetic acid was necessary for the formation of high valent nickel complexes with NaOCl. Addition of acetic acid (4.5 equiv.) to **3** in acetonitrile (generated by addition of 4.5 equiv. of NaOCl to **1** (0.9 mM)) did not affect the absorbance at 612 nm significantly (Figure S21a). In contrast, addition of acetic acid (4.5 equiv.) prior to addition of NaOCl to **1** (0.9 mM) precluded the appearance of the 612 nm band and hence formation of **3** (Figure S21b).[17]

The ESI mass spectra of **1** in acetonitrile show signals (m/z) assignable to [Ni(II)(L)(CH$_3$CN)$_2$]$^{2+}$ (155.9 m/z), [Ni(II)(L)(CH$_3$CN)$_3$]$^{2+}$ (176.3 m/z), [Ni(II)(L)(Cl)]$^+$ (264.1 m/z) and [Ni(II)$_2$(L)$_2$(Cl)$_3$]$^+$ (565.2 m/z) (Figure S3). The spectrum obtained from a solution containing **3** shows an additional strong signal at 253.3 m/z with an isotope distribution consistent with two Ni centers (Figure S22), regardless of whether it was generated with NaOBr or NaOCl and with **2** in place of **1** (Figure S22-27). Notably, however the signal increased by 3 m/z units with Na^{18}OCl (Figure S24). The m/z signal at 253.3 is therefore consistent with structures such as the peroxy bridged **3a** [(L)$_2$Ni(III)$_2$(μ-O)(μ-O-O)]$^{2+}$ and the tri-μ-oxido bridged **3** [((L)$_2$Ni(IV)$_2$(μ-O)$_3$]$^{2+}$, with the latter structure favored on the basis of by Raman spectroscopy (vide infra) and DFT. All possible spin states were explored by DFT methods for both **3** and **3a**. As expected for the d^6 Ni(IV) ions in **3**, the lowest energy[13] state is S = 0 with the other spin states lying > 27 kcal·mol^{-1} higher in energy.
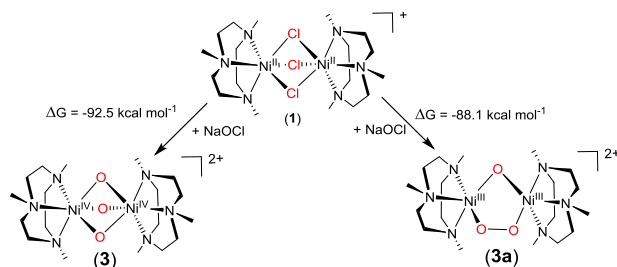

Figure 2 Structures (**3, 3a**) consistent with ESI mass spectral data and calculated driving forces for their formation from **1**.

For the d^7 Ni(III) ions in **3a**, the lowest energy[13] state is a doublet on each of the metals which are ferromagnetically (S = 1) or antiferromagnetically (open-shell singlet) coupled. The open-shell singlet is lower in (Gibbs free) energy than the triplet by 2.1 kcal·mol^{-1},

and 5.1 kcal·mol^{-1} lower than the closed-shell singlet state. All other spin states for **3a** are >10 kcal·mol^{-1} higher in (Gibbs free) energy.
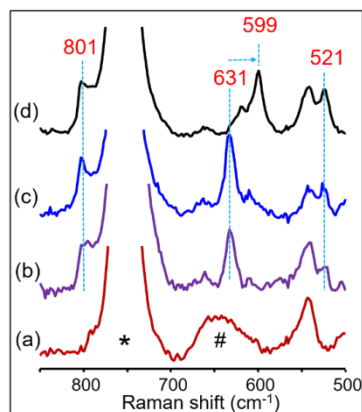

Figure 3 Raman spectra (λ_{exc} 532 nm) of **1** (3.5 mM) in acetonitrile (a) and with (b) 4.5 equiv. of NaOBr, (c) 4.5 equiv. of Na^{16}OCl and (d) 4.5 equiv. of Na^{18}OCl. *Solvent band. # Raman band from quartz.

The Raman spectrum of **3**, with excitation resonant with the visible absorption band, shows enhanced Raman scattering at 801, 631, and 521 cm^{-1} (Figure 3), with only the band at 631 cm^{-1} ($\Delta[^{18}O]$ = 32 cm^{-1}) affected by the use of Na^{18}OCl. The bands are unaffected by use of OBr$^-$ in place of OCl$^-$. The DFT calculated Raman spectrum for $[(L)_2Ni(IV)_2(\mu\text{-}^{16/18}O)_3]^{2+}$ (**3**) shows a symmetric stretching Ni-O-Ni mode at 638 cm^{-1} shifted to 609 cm^{-1} (i.e. $\Delta[^{18}O]$ = 29 cm^{-1}, Figure S29). The band at 801 cm^{-1} (calc. by DFT at 782 cm^{-1}) corresponds to a symmetric Ni-N stretching, while the band at 521 cm^{-1} (calc. by DFT at 517 cm^{-1}) involves both Ni-N and Ni-Ni stretching (see SOI). The modes are similar in energy to those of the isostructural complex $[(L)_2Mn(IV)_2(\mu\text{-}O)_3]^{2+}$, which shows a Mn-O-Mn stretch at 701 cm^{-1} ($\Delta^{18}O$ = 33 cm^{-1}).[18] Furthermore, the spectrum is similar to that reported by Riordan and co-workers for $[((PhTt^{tBu})Ni(III))_2(\mu\text{-}O)_2]$ with a band at 585 cm^{-1} ($\Delta[^{18}O]$ = 30 cm^{-1}),[19] and by Fukuzumi and co-workers for $[(L'Ni(III))_2(\mu\text{-}O)_2]^{2+}$, where L' = *N,N*-bis[2-(2-pyridyl)ethyl]-2-phenylethylamine, with a band at 612 cm^{-1} ($\Delta[^{18}O]$ = 32 cm^{-1}).[20] The higher Raman shift for **3** is consistent with an increase in the oxidation state from III to IV.

Although the ESI mass spectral data could correspond also to a peroxy bridged species (**3a**), the Ni-O-O-Ni stretching modes are expected at higher wavenumbers compared to Ni-O-Ni modes; see, for example, the O-O stretch vibrations reported by Riordan and co-workers ($[(Ni(tmc))_2(\mu\text{-}O\text{-}O)]$ at 778 cm^{-1} ($\Delta[^{18}O]$ = 43 cm^{-1}),[21] and Gade and co-workers $[(Ni(iso\text{-}pmbox))_2(\mu\text{-}O\text{-}O)]$ (742 cm^{-1}, $\Delta[^{18}O]$ = 36 cm^{-1}).[22] This conclusion is supported by the DFT calculated IR spectrum for **3a** (Figure S30) which shows an O-O stretching band ($\Delta[^{18}O]$ in parentheses) at 892 (841) cm^{-1}, Ni-N stretching mode at 768 (768) cm^{-1}, and Ni-O bending/stretching modes at 663 (633) cm^{-1}, 601 (594) cm^{-1}, 585 (571) cm^{-1} and 536 (516) cm^{-1}. Of these modes, the 663 and 768 cm^{-1} modes are strongly IR active. Therefore, given that in the present system only the band at 631 cm^{-1} is affected by the use of ^{18}OCl$^-$, and that the DFT calculated IR spectrum of **3a** (Figure S30) indicates bands at ca. 660 and 770 cm^{-1} only and not a band at ca. 801 cm^{-1}, then the most appropriate structural assignment for the high valent nickel species is **3**.

DFT calculations provide further support for this assignment in the thermochemistry of the reaction of **1** and **2** with NaOCl to form **3**. Mass spectral data indicate that the reactive intermediate **3** has the composition $[(L)_2Ni_2O_3]^{2+}$, and the absence of EPR (X-band) signals at 77 K at any time suggests that mononuclear Ni(III) complexes are not present to a significant extent. Hence, geometry optimizations were performed with all spin multiplicities for **1**, **2**, **3** and **3a**, as well as possible mononuclear Ni(II) complexes, e.g., $[(L)Ni(II)(CH_3CN)_3]^{2+}$ (**4**), and $[(L)Ni(II)(CH_3CN)_2]^{2+}$ (**5**) (Tables S2). Anti-ferromagnetically coupled dinuclear species were found as lowest energy for **1**, **2** and **3a**, while a closed-shell spin state was found for **3** (*vide supra*). A high-spin Ni(II) (S=1) ground state was found for **4** and **5**. The reaction of **1** with NaOCl to form **3** or **3a** (Scheme 2) were calculated to be exergonic by -92.5 kcal·mol^{-1}, and -88.1 kcal·mol^{-1}, respectively, and hence **3** is 4.46 kcal·mol^{-1} more stable than **3a** in terms of Gibbs energy (7.50 kcal·mol^{-1} in electronic energy), Table S3.

Overall, the spectroscopic and computational data are consistent with the assignment of the intermediate as **3** ($[(L)_2Ni(IV)_2(\mu\text{-}^{16}O)_3]^{2+}$). The mechanism by which **3** forms from Ni(II) complexes undoubtedly involves multiple elementary steps. However, the coordination of OCl$^-$ to Ni(II) is expected to be facile given the rapid exchange of Cl$^-$, Br$^-$ and CH$_3$CN ligands. Heterolytic cleavage of Ni(II)-O-Cl to form a transient intermediate Ni(IV) species and Cl$^-$ is presumably followed by formation of a (μ-O)$_3$ bridged Ni(IV) dimer in which anti-ferromagnetic coupling of the Ni(IV) centers provides stabilization.
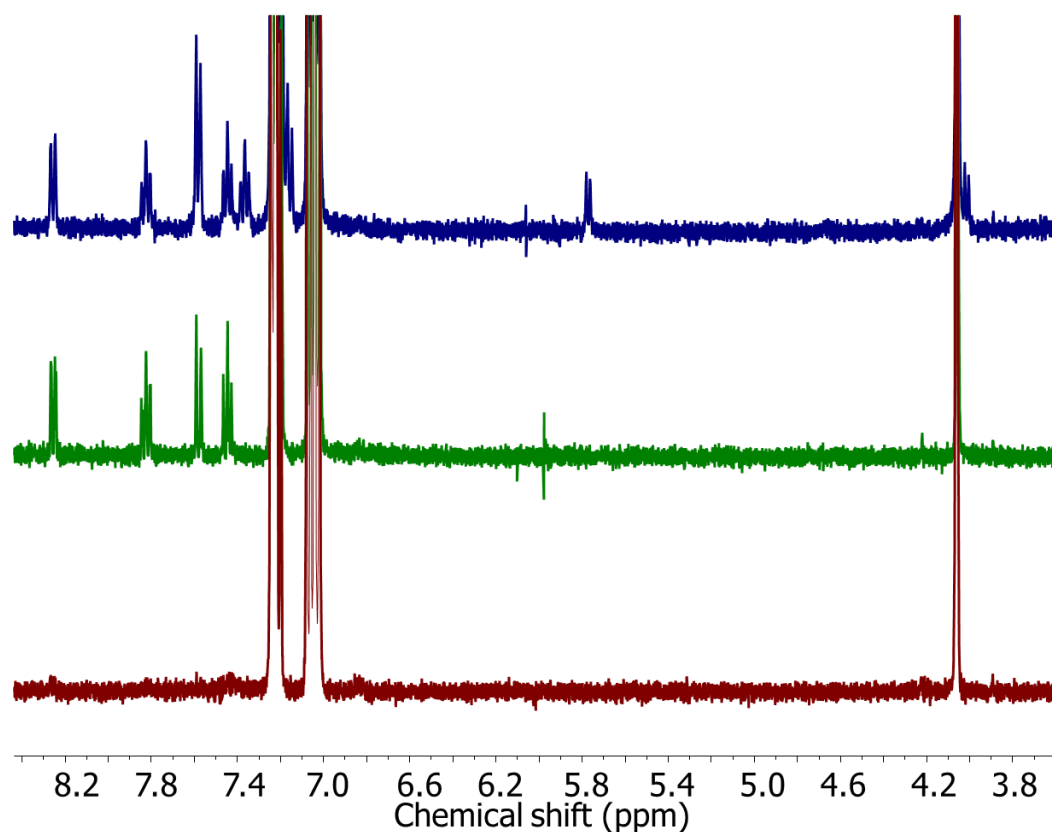

Figure 4 ^{1}H NMR spectrum of xanthene (18 mM in CD$_3$CN) before (red) and after addition of NaOCl (18 mM, green) and after addition of **1** (3.48 mM) followed by addition of NaOCl (18 mM, blue).

Finally, although **3** undergoes rapid self-decay in methanol to yield formaldehyde, in acetonitrile it is relatively stable allowing for its reactivity with organic substrates to be assessed. The addition of ca. 4 equiv. substrate (*e.g.*, xanthene, 9,10-dihydroanthracene and fluorene) resulted in a complete loss of absorbance at 612 nm within c.a. 6 min (70 s, 150 s, and 350 s, respectively, Figure S31). At -15 °C, **3** is stable for over 6 h (Figure S32), however, addition of 4 equiv. xanthene resulted in a rapid loss in absorbance at 612 nm (within c.a. 275 s, Figures S33). The ^{1}H NMR spectrum of the reaction mixture shows signals from xanthene, and weak signals at 5.7, 7.1, 7.4, 7.6, 7.8, 8.3 ppm, and for the reaction (without **1**) at 7.4, 7.6, 7.8, 8.3 ppm, indicating that, in the presence of **1,** a mixture of products were formed (Figure 4). Addition of 50 equiv. fluorene to **3** resulted in the disappearance of the signal at m/z 253.3 and a recovery of the signals of **1** and **4** (Figure S34). Hence, although substrates react directly with NaOCl, **3** engages in C-H oxidation also.

5.3 Conclusions

In conclusion, complex **3** represents the first example of a Ni(IV) oxido bridged dimer. Its generation from NaOCl and subsequent reaction with organic substrates opens up the possibility to use NaOCl as a terminal oxidant. The intermediacy of a transition metal catalyst opens the possibility of engaging in selective oxidations, thereby taming the reactivity of this potent oxidant.

5.4 Experimental section

The ligands 1,4,7-trimethyl-1,4,7-triazacyclononane (TMTACN) was obtained from CATEXAL. Commercially available chemicals were purchased and used without further purification. Aqueous NaOCl (10 - 15 %) was obtained from Sigma Aldrich. Na^{18}OCl was prepared by diluting aqueous NaOCl in H$_2$^{18}O (1:7 v/v).

^{1}H NMR spectra measurements (400 MHz) were recorded on a Varian Mercury Plus. Chemical shifts are assigned relative to solvent peak (^{1}H NMR spectra CD$_3$CN, 1.94 ppm). UV/Vis absorption spectra were recorded with a Specord600 (AnalytikJena) in 10 mm path length quartz cuvettes. X- band EPR spectra were recorded on a Bruker ECS106 spectrometer in liquid nitrogen (77 K). Samples for measurement (300 μL) were transferred to EPR tubes, were flash frozen in liquid nitrogen immediately. ESI-MS spectra recorded on a Triple Quadrupole LC/MS/MS mass spectrometer (API 3000, Perkin-ElmerSciex Instruments). Elemental analyses were performed with a Foss-Heraeus CHN Rapid or a EuroVector Euro EA elemental analyzer. Solid state Raman spectra were recorded at λexc 785 nm using a Perkin Elmer Raman Station at room temperature. Raman spectra for following reactions were collected at 532 nm (300 mW at source, Cobolt Lasers) in a 180° backscattering setup. Raman scattering collected by a 2.5 cm diameter plano-convex lens (f = 7.5 cm). The collimated Raman scattering passed through an appropriate long pass edge filter (Semrock) and was focused by a second 2.5 cm diameter plano convex lens (f = 10 cm) into a Shamrock300i spectrograph (Andor Technology) with a 2399 L/mm grating blazed at 300 nm, acquired with an iDus-420 CCD camera (Andor Technology). The spectral slit width was set to 50 μm. Data were recorded and processed using Solis (Andor Technology) with spectral calibration performed using the Raman spectrum of acetonitrile/toluene 50:50 (v:v). Samples were held in quartz 10 mm path length cuvettes. Baseline correction was performed for all spectra.

[Ni^{II}$_2$(TMTACN)$_2$(μ-Cl$_3$)]Cl.(H$_2$O)$_5$ (**1**) 1409 mg of NiCl$_2$.6H$_2$O (5.92 mmol) were dissolved in 30 ml of DMSO in an open crucible at 190ºC, followed by evaporation to c.a.2/3 of its original volume. After cooling TMTACN (1012 mg, 5.90 mmol) in 10 ml of ethanol was added. Then the solution was heated again, providing green crystals which were washed with methanol and diethyl ether. A trituration with CH$_2$Cl$_2$ was followed by recrystallization from methanol/diethyl ether. After filtering and air drying, complex **1** was obtained as a green/blue powder, yield 58.8 %, elemental analysis experimental C - 30.74 %, H - 7.56 %, N - 11.83 %. Calculated with 5 water molecules C - 30.46 %, H - 7.67 %, N - 11.84 %. Karl Fisher titration and FTIR spectroscopy indicates 16 wt% water of crystallization.

[Ni^{II}$_2$(TMTACN)$_2$(μ-Br$_3$)]Br.(H$_2$O)$_8$ (**2**) 887 mg of NiBr$_2$ (4 mmol) were dissolved in 30 ml of DMSO in an open crucible at 190º C, followed by evaporation to c.a.2/3 of its original volume. After cooling TMTACN (696 mg, 4 mmol) in 10 ml of ethanol was added. Then the solution was heated again, providing green crystals which were washed with methanol and diethyl ether. A trituration with dichloromethane was then performed followed by recrystallization with methanol/diethyl ether. After filtering and air drying, complex **1** was obtained as a green/blue powder. yield 55%, elemental analysis experimental C - 23.49 %, H - 6.21 %, N - 9.05 %. Calculated with 8 water molecules - C - 23.41%, H - 6.33%, N - 9.10%.

Table 1 ^{1}H NMR (chemical shifts), UV-vis absorption (ε) and ESI mass spectroscopy (m/z) values of complexes **1** and **2**.

complex	^{1}H NMR	UV-vis	ESI-MS (m/z)
1	60 ppm (s, broad), 90 ppm(s, broad), 120 ppm (s, broad)	384 (ε = 18 M^{-1} cm^{-1}), 635 (ε = 9 M^{-1} cm^{-1})	[(TMTACN)$_2$Ni(II)$_2$(Cl)$_3$]$^+$ (565.3).
2	60 ppm (d, broad), 92 ppm (s, broad), 119 ppm (d, broad)	388 (ε = 20 M^{-1} cm-1), 640 (ε = 9 M^{-1} cm^{-1})	[(TMTACN)$_2$Ni(II)$_2$(Br)$_3$]$^+$ (699)

[Ni^{II}(TMTACN)(CH$_3$CN)$_3$]$^{2+}$ (**4**) Addition of 10 equiv. of NaOCl to **1** in acetonitrile followed by addition of saturated KPF$_6$ and recrystallization from acetonitrile in a diethyl ether bath yielded the mononuclear complex [Ni^{II}(TMTACN)(CH$_3$CN)$_3$]$^{2+}$ (**4**).

5.5 Additional spectral data

5.5.1 Raman, ^{1}H NMR, UV-vis absorption spectroscopy and ESI mass spectrometry of 1 and 2

The Raman spectra of **1** and **2** are similar as expected, except for a several low wavenumber bands (200-300 cm^{-1}) due to differences in Ni-Br and Ni-Cl stretching modes.
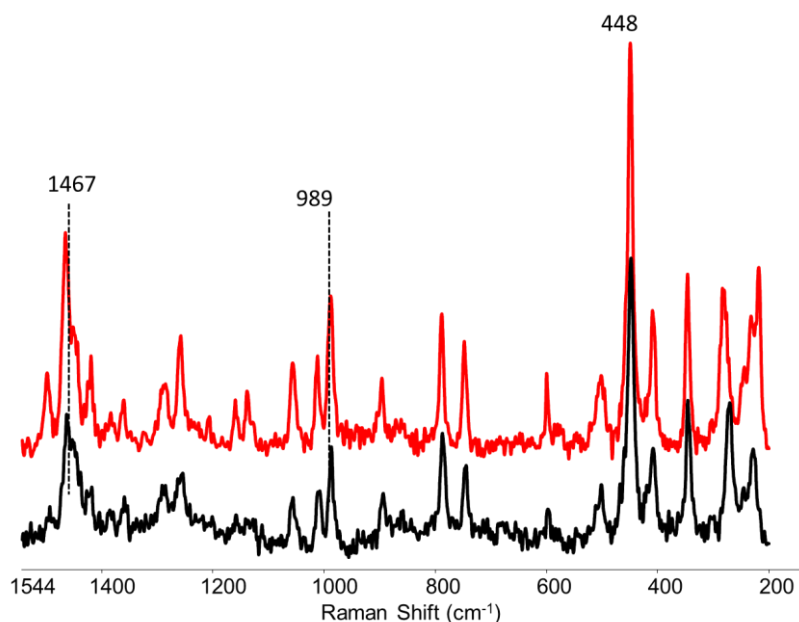

Figure S1 Raman spectrum (λ_{exc} 785 nm) of **1** (red) and of **2** (black) in the solid state.
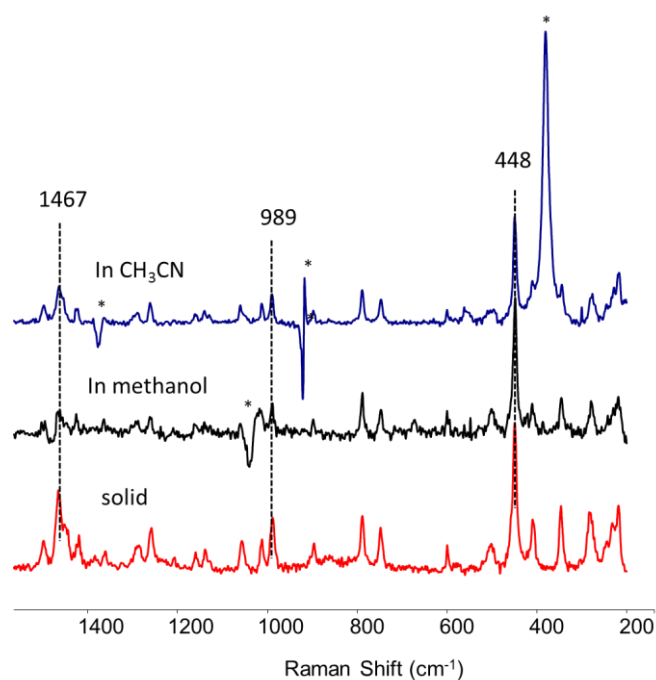

Figure S2 Raman spectrum (λ_{exc} 785 nm) of **1** in the solid state (red) and in methanol (224 mM, black), in acetonitrile (224 mM, blue). *improper solvent subtraction.
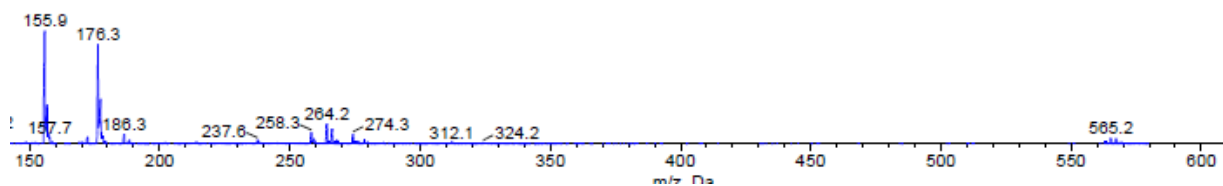
Figure S3 ESI mass spectrum of **1** (0.9 mM) in acetonitrile.
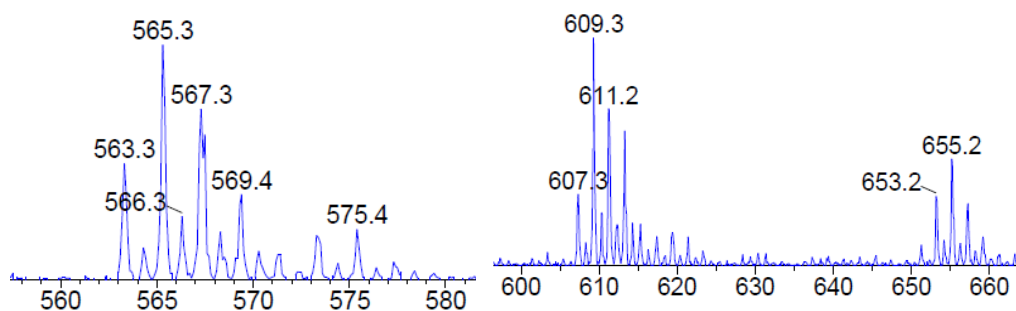
Figure S4 ESI mass spectrum of a mixture of **1** (0.45 mM) and **2** (0.45 mM) in acetonitrile. The 1:1 mixture of **1** and **2** shows m/z signals at $[(L)_2Ni(II)_2(Cl)_3]^+$ (565.3), $[(L)_2Ni(II)_2(Br)_3]^+$ (699), $[(L)_2Ni(II)_2(Br)_2(Cl)]^+$ (655.2), and $[(L)_2Ni(II)_2(Br)(Cl)_2]^+$ (610.7).
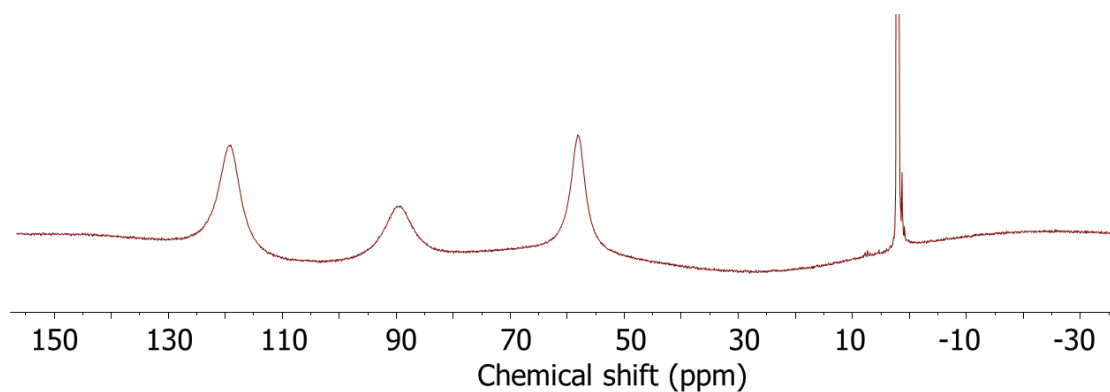

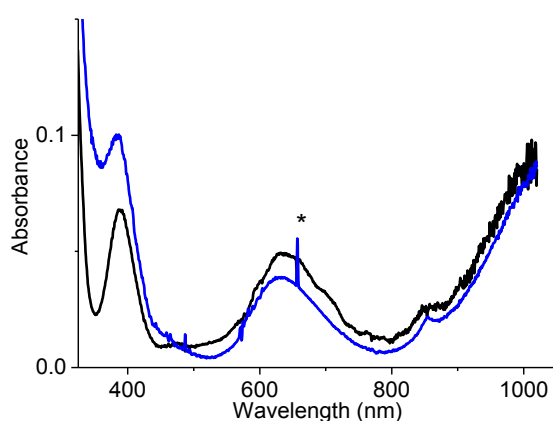**Figure S5** ^{1}H NMR (400 MHz) spectrum of **1** (9 mM) in CD$_3$CN.

Figure S6 UV-vis absorption spectra of **1** (3.5 mM) in methanol (black) and acetonitrile (blue). *instrumental artefact.
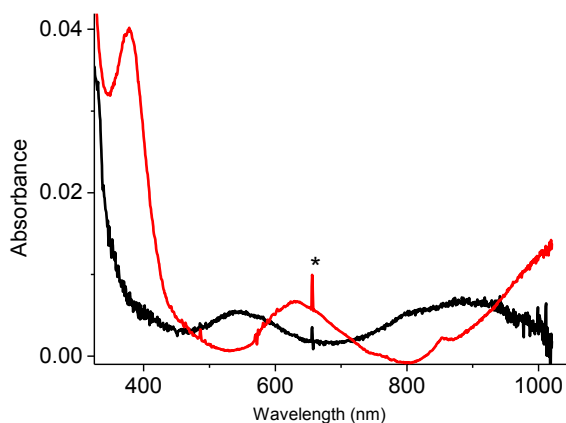
Figure S7 UV-vis absorption spectra of **1** (3.5 mM) in acetonitrile (red), **4** (ca. 0.3 mM) in acetonitrile (black). * instrumental artefact.

5.5.2 Reaction of 1 and 2 in methanol with NaOCl and NaOBr
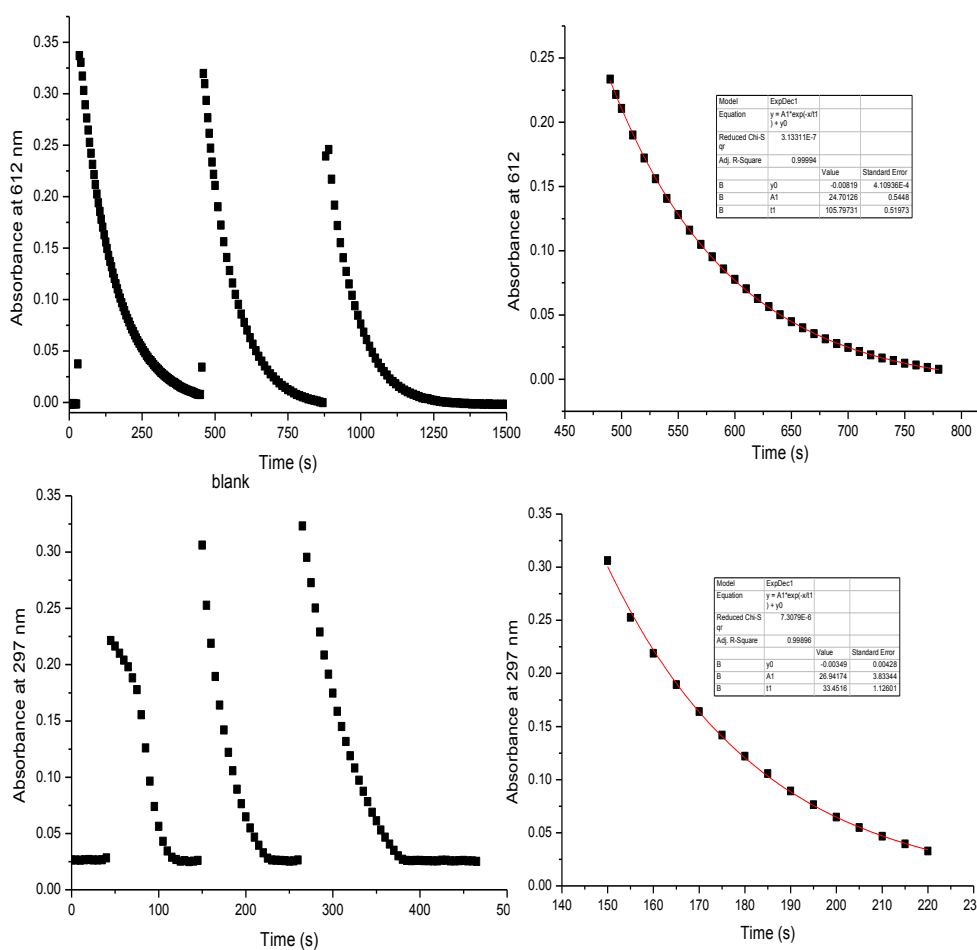

Figure S8 Time dependence of absorbance at (upper) 612 nm with **1** (0.9 mM) and (lower) 297 nm without **1** in methanol after addition of NaOCl (4.5 mM) three times in series. An exponential fit to the second decay trace in each case is shown on the right.

5.5.3 Quantification of formaldehyde formation

Addition of 11 equiv. NaOCl (without **1**) to methanol led to the increase in absorbance at 297 nm, which decreases again over c.a. 1230 s. An analysis of the formaldehyde formed with and without **1** shows that the presence of **1** results in a slight increase in the amount of formaldehyde produced, indicating that intermediate **3** reacts with methanol to form formaldehyde also. The formaldehyde test was performed using as described earlier.[23] The colorimetric reagent was prepared as a solution of NH_4OAc (15 g, 0.19 mol), acetic acid (0.3 cm^3, 5.4 mol) and pentane-2,4-dione (0.2 cm^3, 1.9 mol) in 100 cm^3 of water. The reaction mixture was diluted 20 fold with water and 1 ml of this diluted solution is mixed with 1 ml of colorimetric reagent. The mixture was kept as 31 ºC. After 25 min the absorbance at 412 nm (for 3,5-diacetyl-1,4-dihdrolutidine ε_{412} = 8840 M^{-1} cm^{-1}) was used to calculate the concentration of formaldehyde formed.
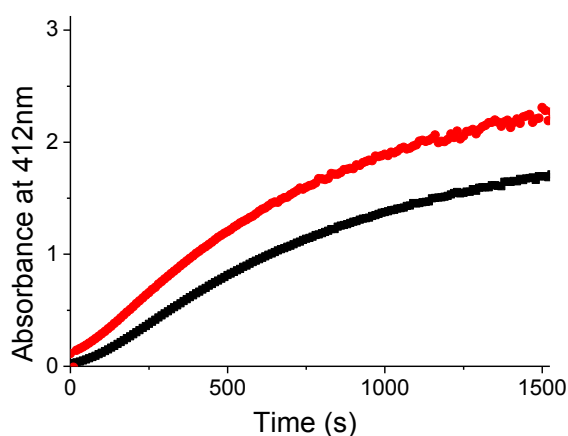

Figure S9 Absorbance at 412 nm in formaldehyde test with **1** (red) and without **1** (black). The reaction mixture comprised of 11 equiv. of NaOCl added to methanol with and without **1** (3.5 mM).
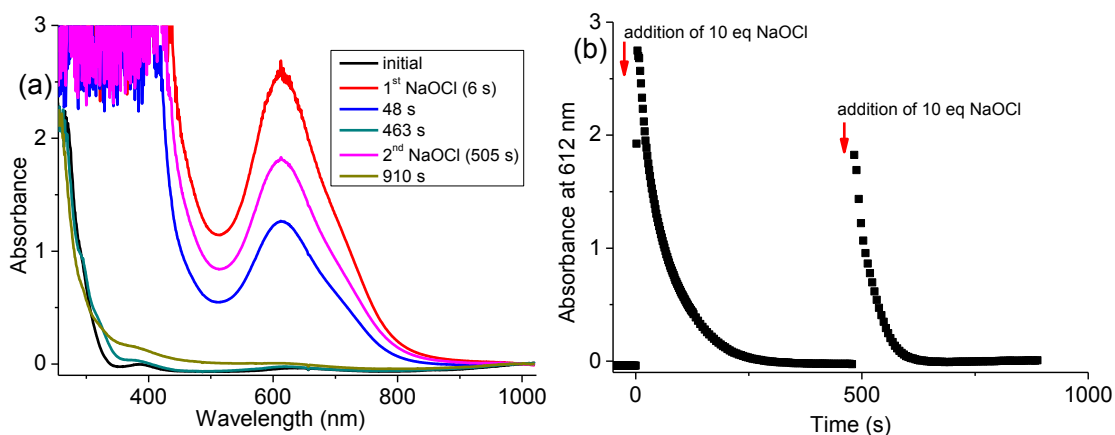

Figure S10 (a) UV-vis absorption spectrum of **1** (3.5 mM) in methanol before (black) and after addition of two batches of 11 equiv. NaOCl. (b) time trace followed at 612 nm.
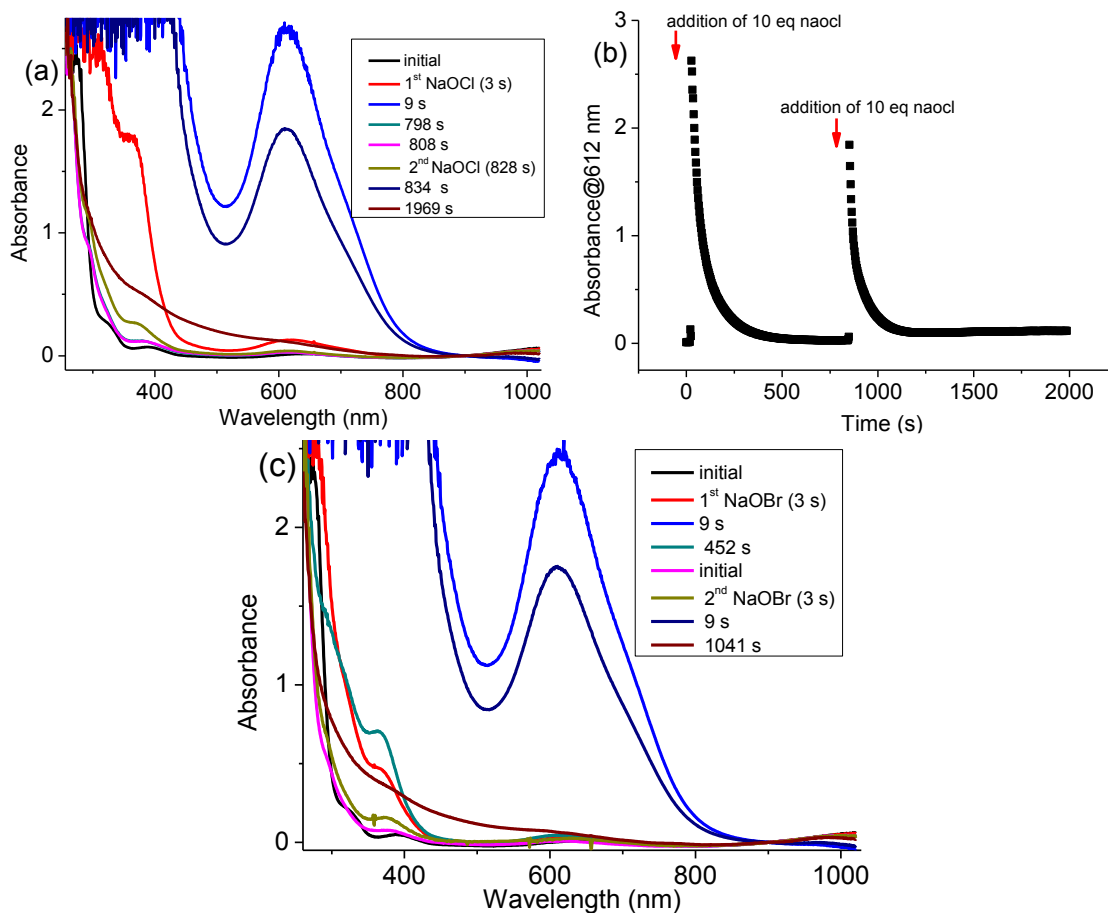
Figure S11 UV-vis absorption spectrum of **2** (3.5 mM) in methanol before (black) and after (a) addition of two batches of 11 equiv. NaOCl, and (b) time dependence of change in absorbance at 612 nm, and (c) before (black) and after addition of two batches of 11 equiv. NaOBr.

5.5.4 Effect of purging with O₂ or addition of H₂O₂ to solutions of 1 in acetonitrile and in methanol
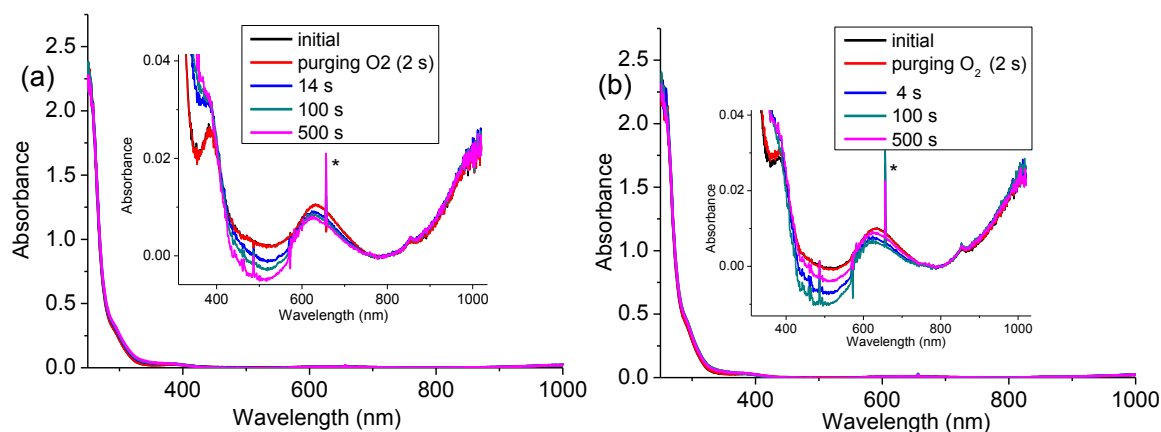

Figure S 12 UV-vis absorption spectra of **1** (0.9 mM) in (a) methanol, and (b) acetonitrile before (black) and during purging with O₂. Inset: expansion of lower absorbance range for clarity.* instrumental artefact.
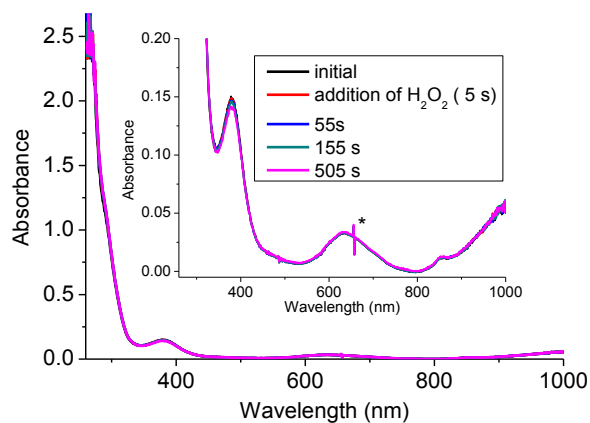
Figure S13 UV-vis absorption spectrum of **1** (3.1 mM) in acetonitrile before (black) and after addition of 7 equiv. of H_2O_2. Inset: expansion of low absorbance range for clarity.* instrumental artefact.
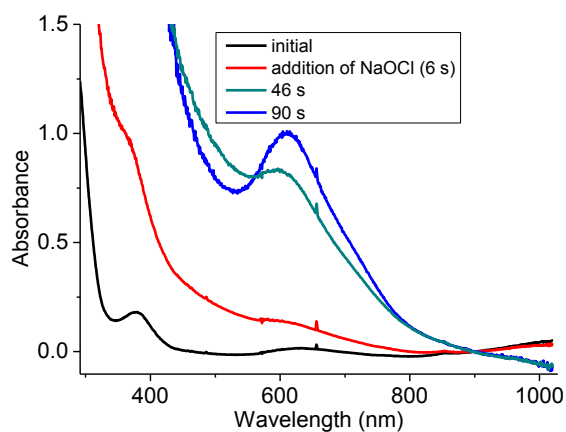

Figure S14 UV-vis absorption spectrum of **1** (3.5 mM) in acetonitrile before (black) and after addition of 11 equiv. NaOCl. Note that the UV-vis absorption spectra are distorted by Mie scattering from precipitated NaCl particles formed from NaOCl.
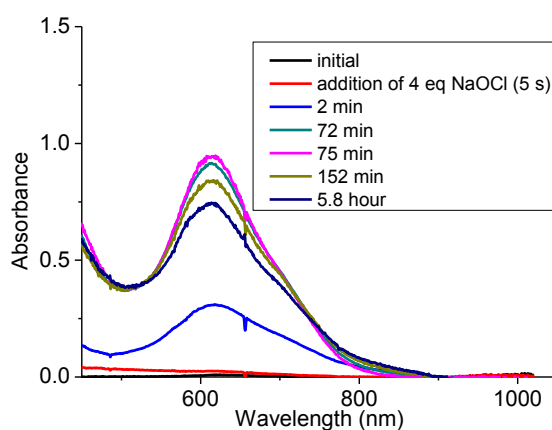

Figure S15 UV-vis absorption spectrum of **1** (0.9 mM) in acetonitrile before (black) and after addition of 4.5 equiv. NaOCl at -15 °C.
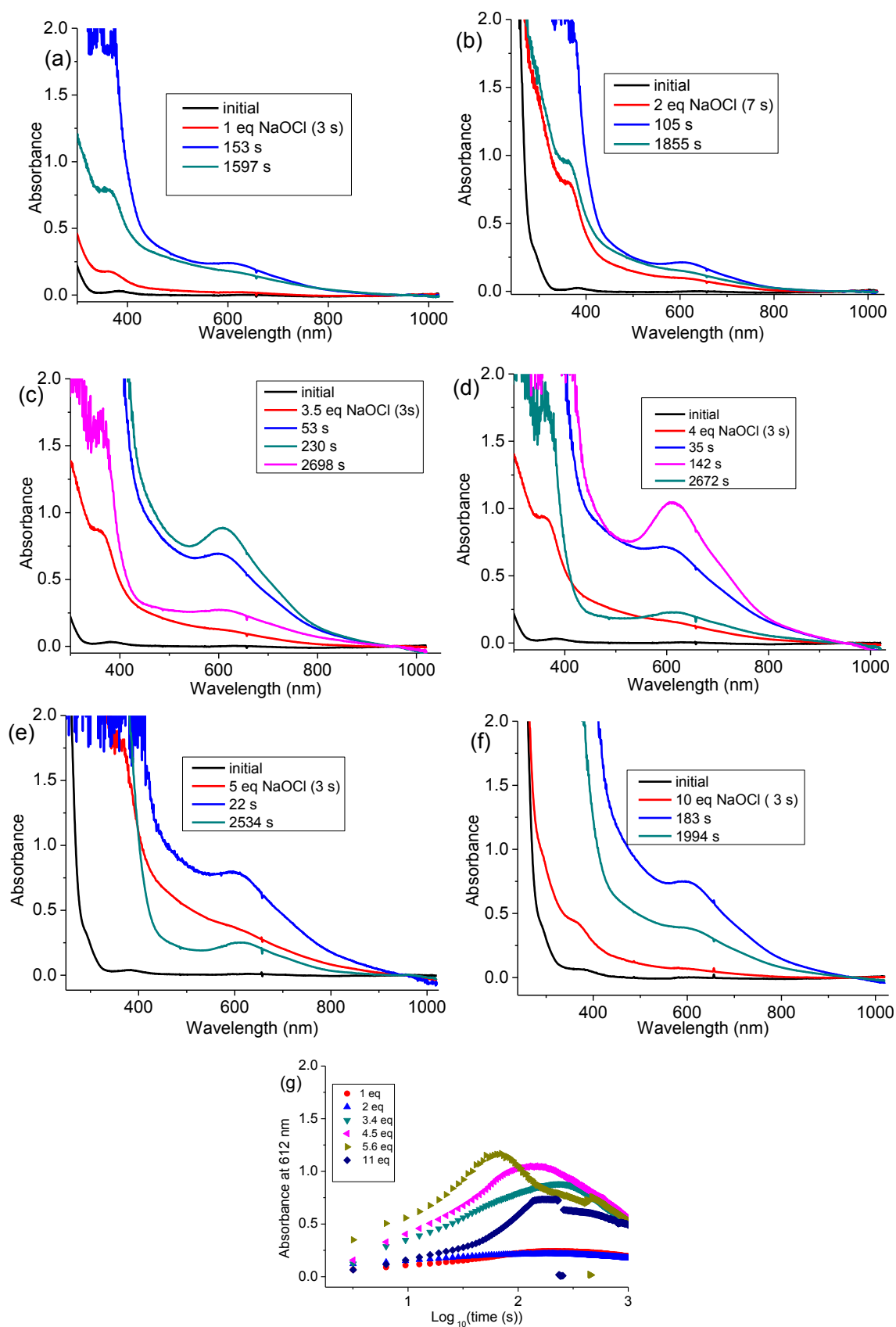
Figure S16 UV-vis absorption spectra of **1** (0.9 mM) in acetonitrile before and after addition of (a) 1 equiv., (b) 2 equiv., (c) 3.5 equiv., (d) 4.5 equiv., (e) 5.5 equiv., (f) 11 equiv. of NaOCl and (g) corresponding time traces followed at 612 nm.
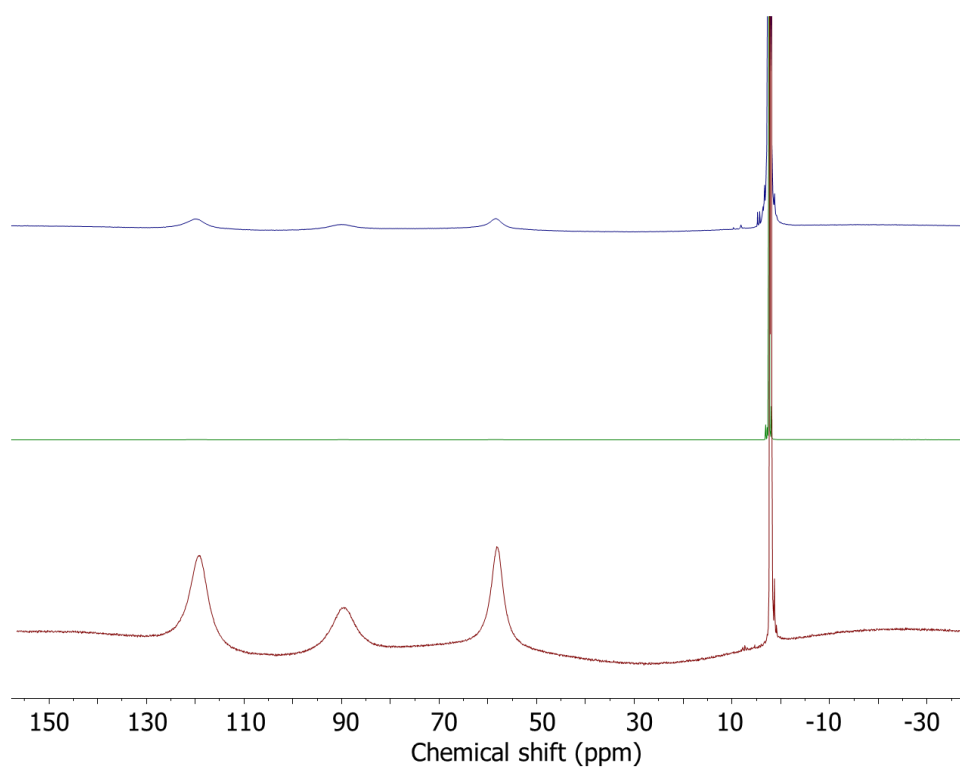
Figure S17 ^{1}H NMR spectra of **1** in CD$_3$CN (9 mM) before (red), 5 min after (green) addition of 4 equiv. NaOCl, and after 3 h (blue).
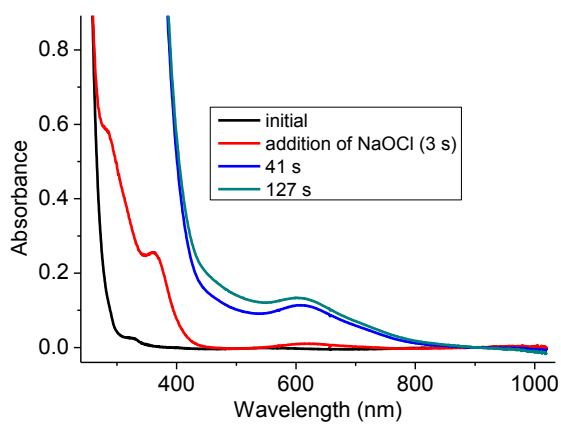

Figure S18 UV-vis absorption spectrum of **4** (ca. 0.3 mM) in acetonitrile before (black) and after addition of 30 equiv. NaOCl.

Figure S19 UV-Vis absorption spectrum of a mixture of NiCl₂.6H₂O (4 mM) and ligand (L) (4 mM)) in acetonitrile before (black) and after (a) addition of 4 equiv. NaOCl, (b) addition of 10 equiv. NaOCl.
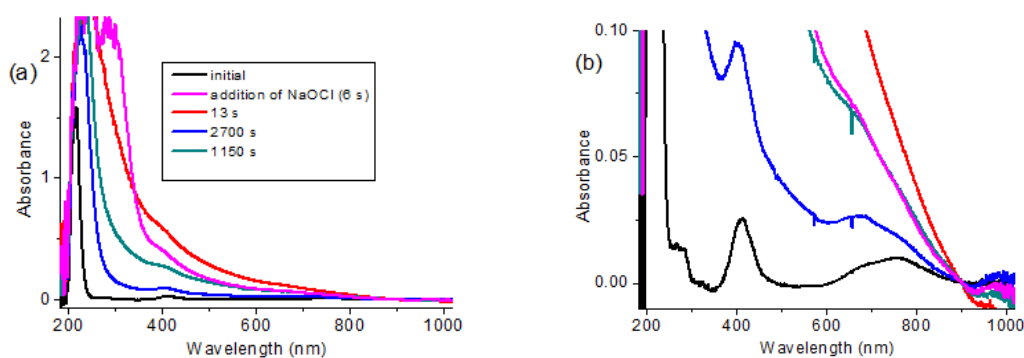
Figure S 20 UV-vis absorption spectrum of NiCl₂.6H₂O (4 mM) in methanol before (black) and after addition of 10 equiv. NaOCl, (a) full spectral range, (b) expansion of (a).

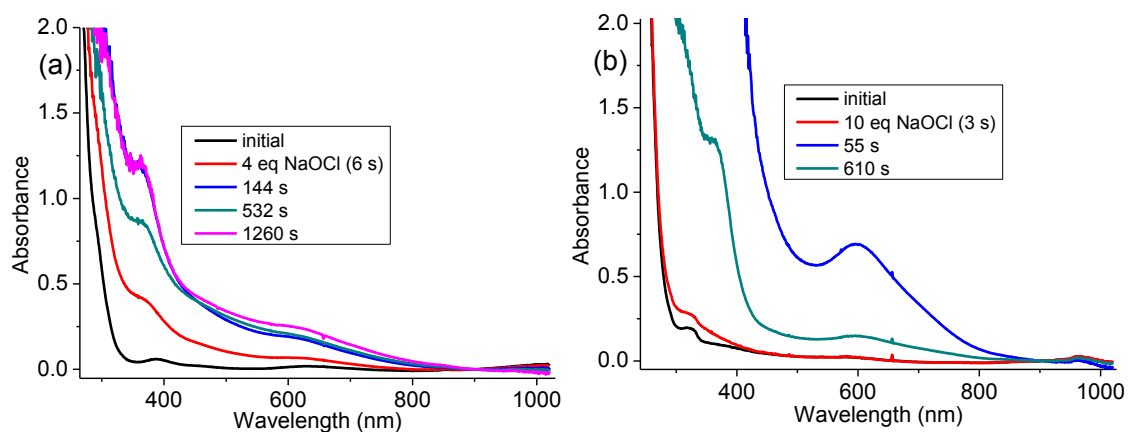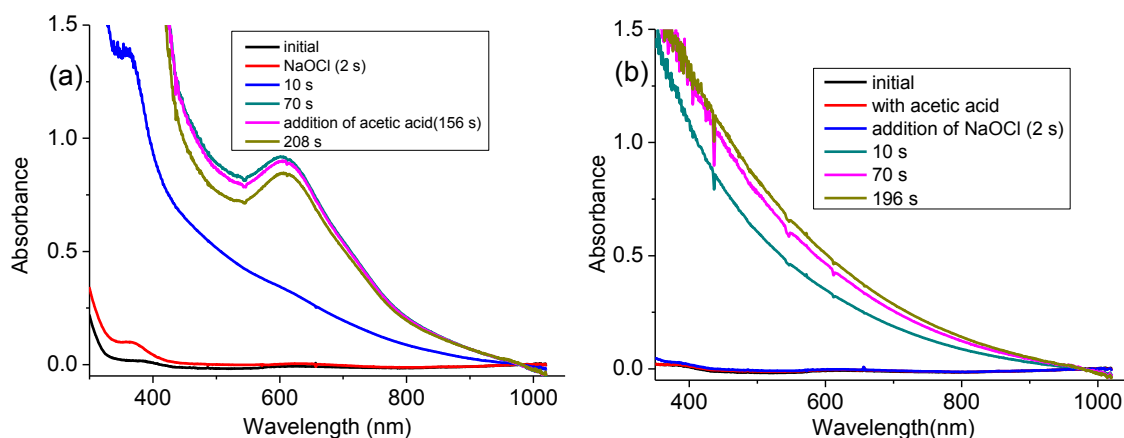**Figure S21** UV-vis absorption spectrum of **1** (0.9 mM) in acetonitrile before (black) and after (a) addition of 4.5 equiv. NaOCl followed by 4.5 equiv. of CH₃CO₂H, and (b) addition of 4.5 equiv. CH₃CO₂H followed by 4.5 equiv. NaOCl, showing only Mie Scattering from precipitated NaCl.

5.5.5 ESI mass spectrometry

Table S2 Assignment of signals observed by ESI mass spectrometry in the m/z spectra.

m/z observed	Assigned to
155.9	$[(L)Ni(II)(CH_3CN)_2)]^{2+}$
176.3	$[(L)Ni(II)(CH_3CN)_3]^{2+}$
565.2	$[(L)_2Ni(II)_2(Cl)_3]^+$
253.3	$[(L)_2Ni(IV)_2(^{16}O)_3)]^{2+}$
264.1	$[(L)Ni(II)(Cl)]^+$
256.3	$[(L)Ni(III)(^{18}O)_3Ni(IV)(L)]^{2+}$
310.1	$[(L)Ni(III)(Cl)(HCO_2)]^+$
374.2	$[(L)Ni(II)(PF_6)]^+$
699.0	$[(L)_2Ni(II)_2(Br)_3]^+$
655.2	$[(L)_2Ni(II)_2(Br)_2(Cl)]^+$
610.7	$[(L)_2Ni(II)_2(Br)(Cl)_2]^+$
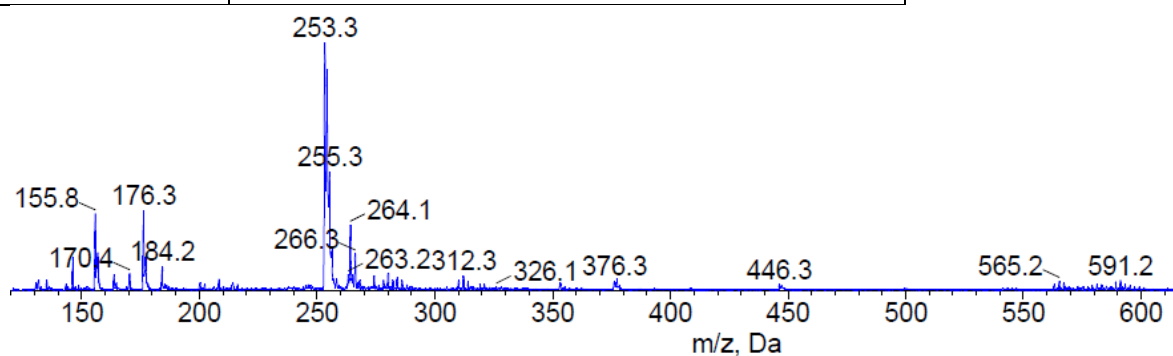
Figure S22 ESI mass spectrum of **1** (0.9mM) in acetonitrile after addition of 5.5 equiv. of Na^{16}OCl.
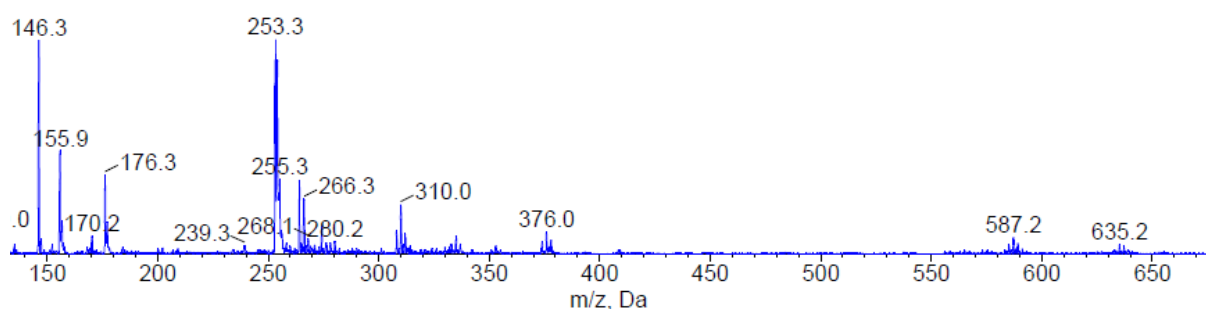
Figure S 23 ESI mass spectrum of **1** (0.9mM) in acetonitrile after addition of 5.5 equiv. of Na^{16}OBr.
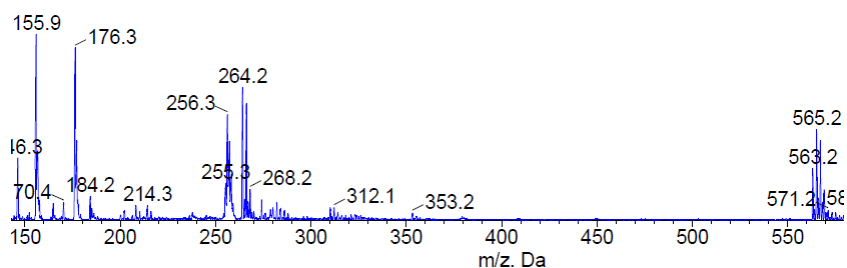
Figure S24 ESI mass spectrum of **1** (0.9mM) in acetonitrile after addition of 5.5 equiv. of Na^{18}OCl.
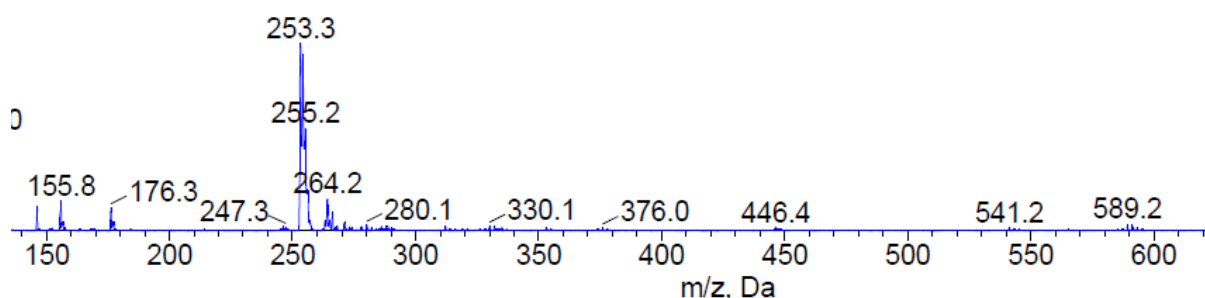
Figure S25 ESI mass spectrum of **2** (0.9mM) in acetonitrile after addition of 5.5 equiv. of Na^{16}OCl.
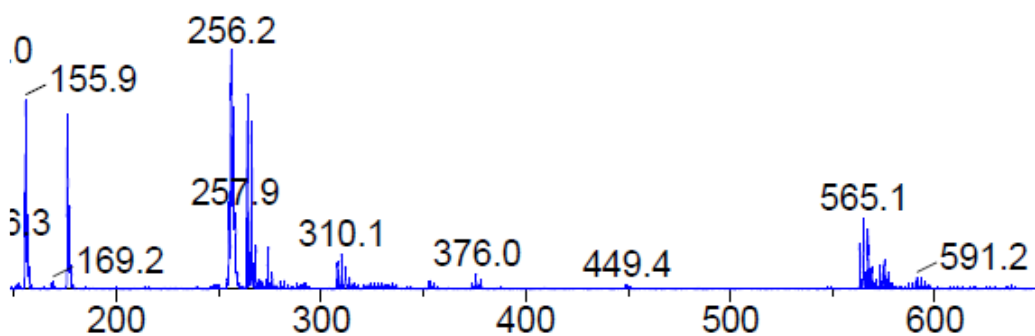
Figure S26 ESI mass spectrum of **2** (0.9mM) in acetonitrile after addition of 5.5 equiv. of Na^{18}OCl.
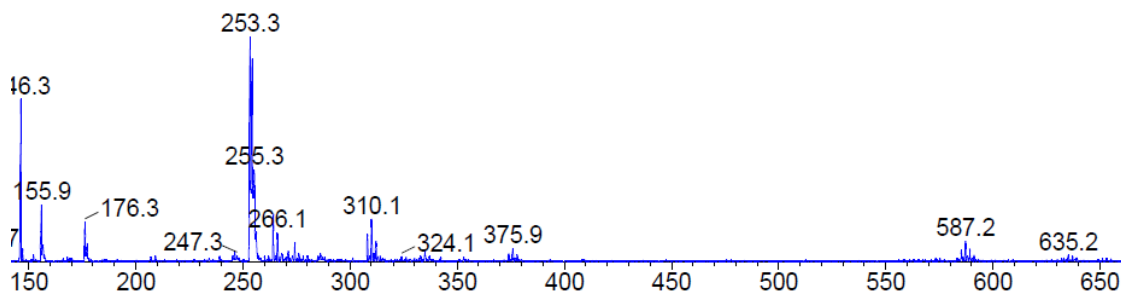
Figure S27 ESI mass spectrum of **2** (0.9mM) in acetonitrile after addition of 5.5 equiv. Na^{16}OBr.

123

155.7
253.3
5.2
176.3
177.2
5.2
.7
194.8
256.3
312.2 353.3
390.3
446.4
565.3
589.3
150 200 250 300 350 400 450 500 550 600 650
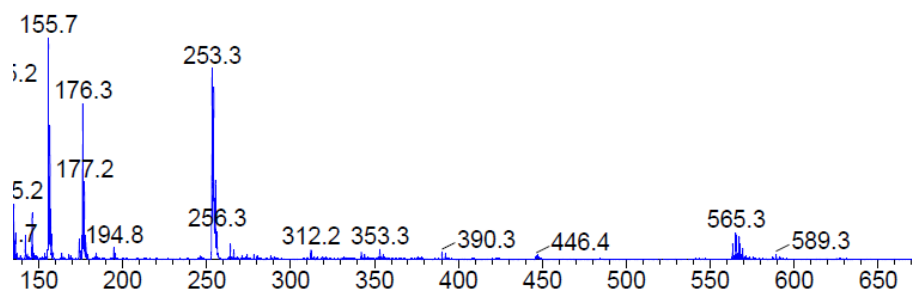
Figure S28 ESI mass spectrum of a mixture of **1** (0.45 mM) and **2** (0.45 mM) in acetonitrile after addition of 5.5 equiv. of $Na^{16}OCl$.
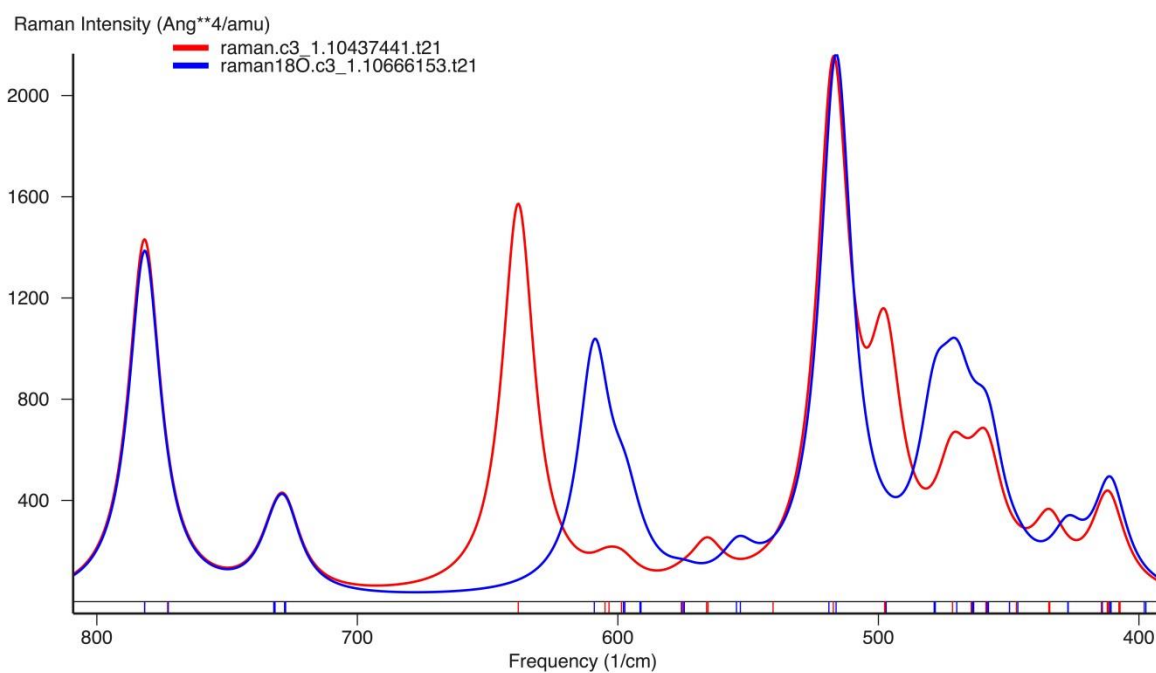
Figure S29 DFT predicted Raman spectra of **3** $[(L)_2Ni(IV)_2(^{16}O)_3)]^{2+}$ (red) and ^{18}O labelled **3** $[(L)_2Ni(IV)_2(^{18}O)_3)]^{2+}$ (blue).
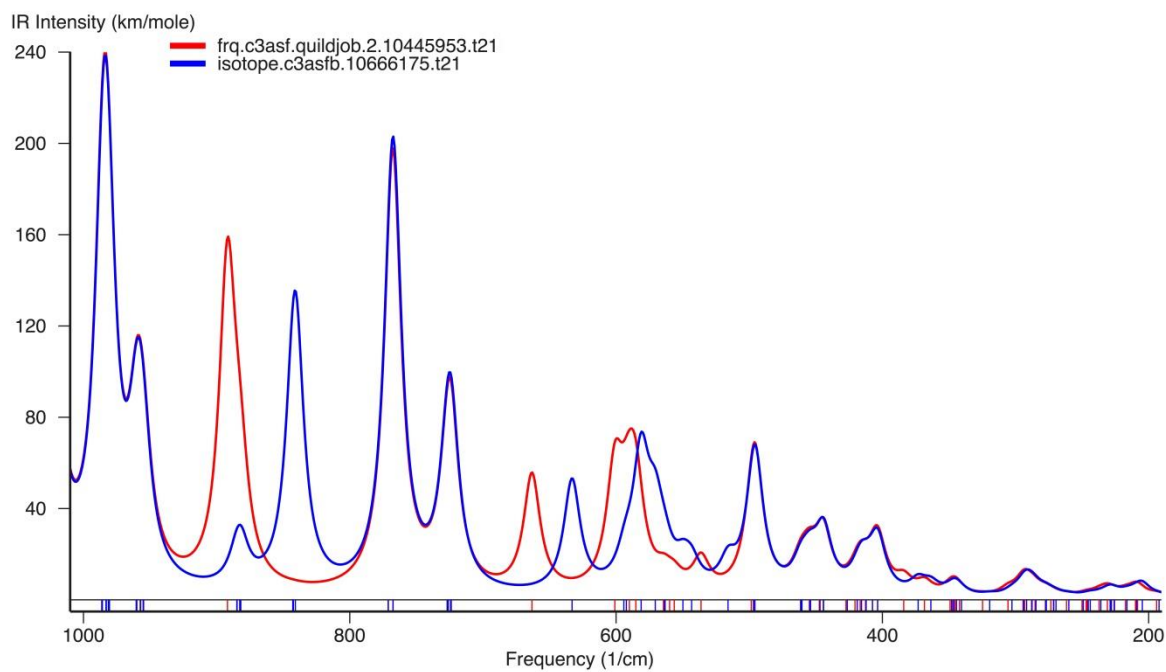
Figure S30 DFT predicted IR spectra of **3a** [(L)$_2$Ni(III)$_2$(^{16}O)$_3$)]$^{2+}$ (red), and ^{18}O labelled [(L)$_2$Ni(III)$_2$(^{18}O)$_3$)]$^{2+}$ (blue).
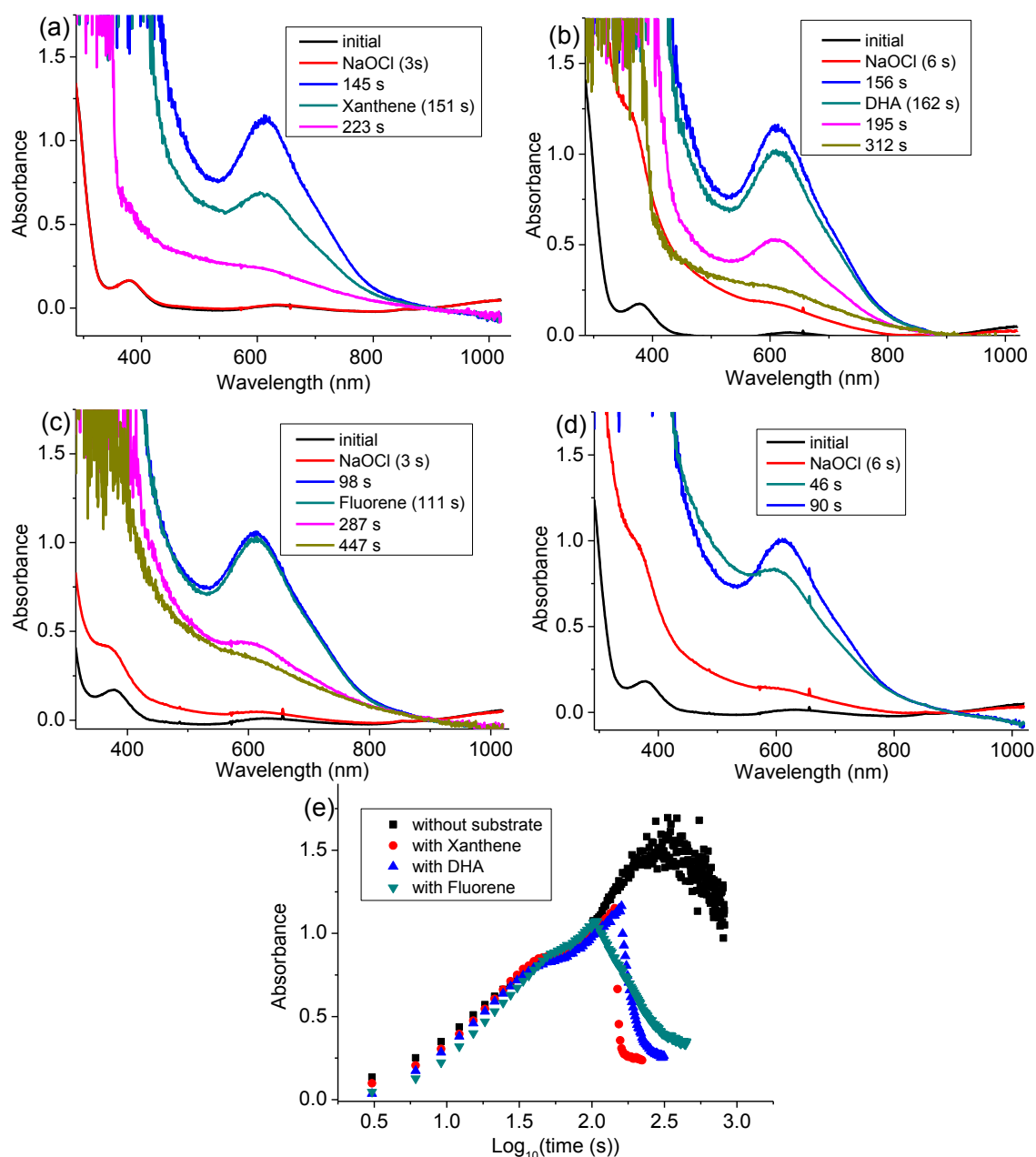
Figure S31 UV-vis absorption spectra of **3** (generated by addition of 5.5 equiv. NaOCl to **1** (3.5 mM)) before (black) and after addition of (a) 4.5 equiv. xanthene , (b) 4.8 equiv. 9,10 – dihydroanthracene (DHA), (c) 4.8 equiv. fluorene (d) addition of 5.5 equiv. and (e) corresponding change in absorbance at 612 nm with (log$_{10}$) time traces compared with self-decay of **3**.
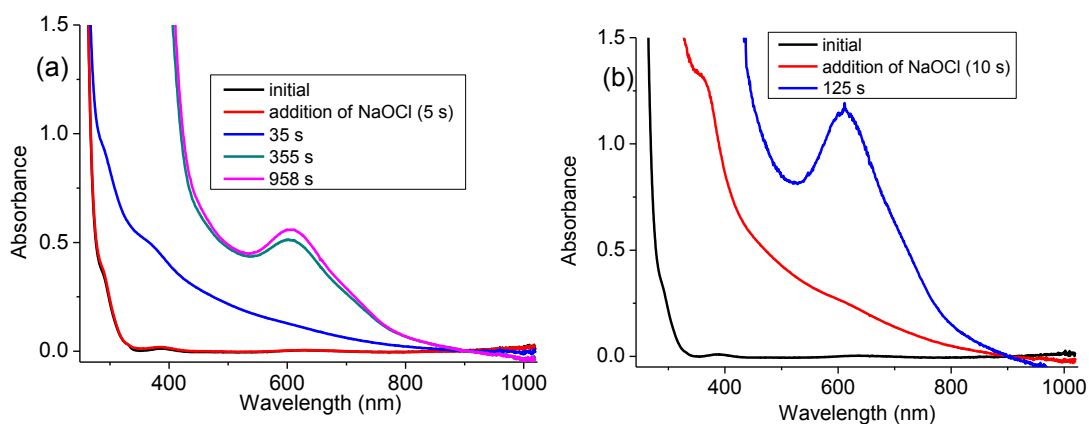
Figure S32 UV-vis absorption spectrum of **1** (0.9 mM) in acetonitrile before (black) and after addition of 4.5 equiv. NaOCl to (a) at -15 °C, (b) at 20 °C.
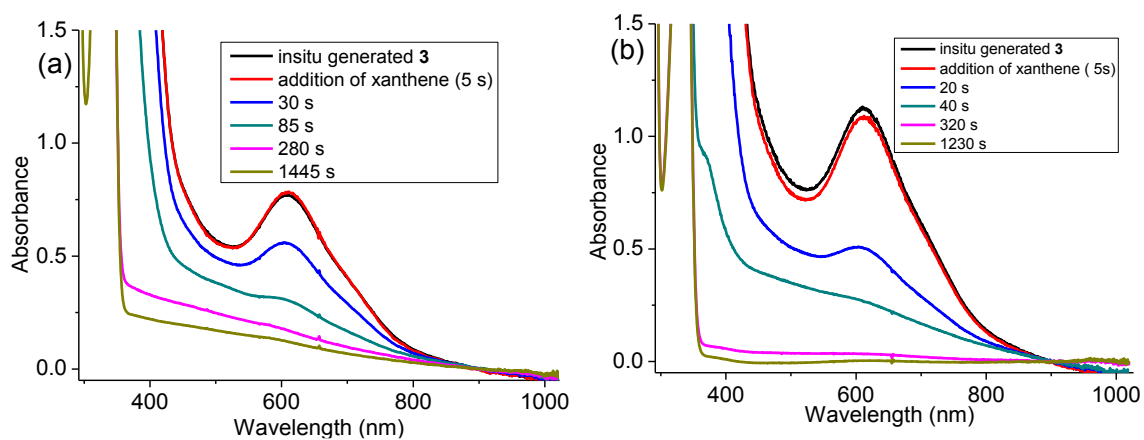
Figure S33 UV-vis absorption spectrum of **3** (generated by addition of 4.5 equiv. NaOCl to **1** (0.9 mM)) before (black) and after addition of 4.5 equiv. xanthene in acetonitrile (a) at -15 °C, (b) at 20 °C.
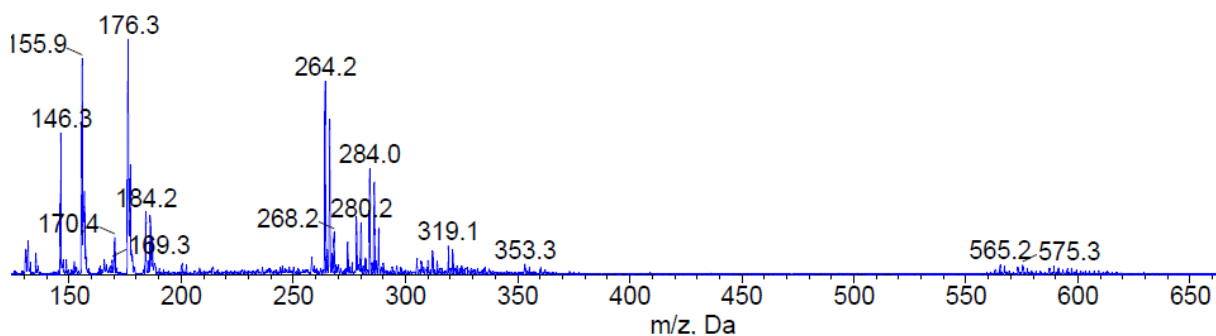
Figure S34 ESI mass spectrum of **3** (generated by addition of 5.5 equiv. Na^{16}OCl to **1** (0.9 mM) in acetonitrile after addition of 5.6 equiv. of fluorene.

5.5.6 DFT Calculations

All DFT calculations were performed with the Amsterdam Density Functional (ADF)[24,25] and QUILD[26] programs. Molecular orbitals were expanded in an uncontracted set of Slater type orbitals (STOs) of triple-ζ quality with double polarization functions (TZ2P), or the TDZP basis set which consists of triple-ζ quality on the metal and double-ζ quality on all other atoms, in both cases including one polarization function.[27,28] Core electrons were not treated explicitly during the geometry optimizations (frozen core approximation[28]). An auxiliary set of s, p, d, f, and g STOs was used to fit the molecular density and to represent the Coulomb and exchange potentials accurately for each SCF cycle.

Geometries of all possible spin states were optimized with the QUILD[26] program using adapted delocalized coordinates until the maximum gradient component was less than 10^{-4} a.u. Energies, gradients and Hessians[29] (for vibrational frequencies, including the Raman intensities) were calculated using BP86-D_3,[12c,30,31] in all cases by including solvation effects through the COSMO[32] dielectric continuum model with appropriate parameters for the solvents.[33] For computing Gibbs free energies, all small frequencies were raised to 100 cm^{-1} in order to compensate for the breakdown of the harmonic oscillator model.[32,33] Scalar relativistic corrections have been included self-consistently in all calculations by using the zeroth-order regular approximation (ZORA).[15] The geometry optimizations at the BP86-D_3 level[34,35] were performed with the TDZP basis set.[36] Subsequent single-point calculations (with the TZ2P basis set) have been performed with S12g,[12a] and all Time-Dependent DFT calculations were carried out with the SAOP potential[37] and the all-electron TZ2P basis set. For all calculations carried out with BP86-D_3 the Becke[34,35] grid of Normal quality was used; calculations performed with SAOP with a Becke grid of Good quality, and S12g calculations were performed with a Becke grid of VeryGood quality.

All DFT calculations were performed using the unrestricted Kohn-Sham scheme. In case of the anti-ferromagnetically coupled systems, a locally adapted version of QUILD was used that allows for geometry optimization using the SpinFlip approach[38] within ADF: at each geometry iteration first a high-spin (all-up) calculation was carried out, from which the orbitals and densities were used to restart (at the same geometry) with the spin densities of one of the Ni atoms change in sign (from spin-up to spin-down) to lead to the open-shell singlet state. The geometry optimization and vibrational frequencies only involve the energy, gradients and Hessians of this second calculation at each (geometry iteration) step.

Table S3 DFT[a] and X-ray[b,c] distances for compounds **1** and **2** (Å)

compound	Ni^A-N (avg)	Ni^A-Cl/Br (avg)	Ni^B-Cl/Br (avg)	Ni^B-N (avg)	Ni^A-Ni^B (avg)
1					
DFT					
S=0	2.145	2.393	2.393	2.145	2.813
S=1	2.125	2.436	2.436	2.125	2.929
S=2	2.110	2.467	2.467	2.110	3.045
AFM	2.114	2.462	2.462	2.114	3.011
X-ray[b]					
NASGIX, mol1	2.117	2.435	2.458	2.103	3.043
NASGIX, mol2	2.107	2.445	2.444	2.109	3.054
2					
DFT					
S=0	2.163	2.538	2.538	2.163	2.972
S=1	2.141	2.583	2.583	2.141	3.102
S=2	2.120	2.623	2.120	2.623	3.248
AFM	2.121	2.621	2.621	2.121	3.235
X-ray[c]					
NASGOD, mol1	2.121	2.593	2.613	2.108	3.234
NASGOD, mol2	2.110	2.596	2.596	2.111	3.242

a) obtained at BP86-D3/TDZP, including COSMO solvation and ZORA relativistic corrections self-consistently; b) ref. 11; c) ref. 11

Table S4 Spin state splittings (E_{elec}, kcal·mol^{-1}) at S12g/TZ2P//BP86-D$_3$/TDZP (incl. COSMO and ZORA)

	S=0 (closed)	S=0 (AFM)	S=1	S=2	S=3	S=4
1	37.70	0.0	25.49	0.32		
2	34.97	0.01	23.43	0.0		
3	0.0	0.0	27.81	41.99	63.16	57.68
3a	11.93	7.50	9.69	18.05	40.13	62.30
4	12.71	0.0				
5	8.47	0.0				

Table S5 Thermodynamic data (kcal·mol^{-1})

Compound	Gibbs Free energy (**G**)	BP86-D$_3$ Electronic Energy (**E$_{BP86}$**)	G-E$_{elec,BP86}$	S12g Electronic Energy (**E$_{S12g}$**)	Total Energy = (**G-E$_{BP86}$ + E$_{S12g}$**)
1^{AFM}	-8400.64	-8747.49	346.85	-8899.29	-8552.44
2^{AFM}	-8366.95	-8711.16	344.21	-8858.78	-8514.57
3^{singlet}	-8480.78	-8837.00	356.22	-8976.00	-8619.78
3a^{AFM}	-8465.37	-8818.55	353.18	-8968.50	-8615.32
4^{triplet}	-6396.71	-6639.61	242.90	-6781.88	-6538.98
5^{triplet}	-5568.02	-5784.97	216.95	-5909.27	-5692.32
NaOCl	-233.48	-217.88	-15.60	-220.32	-235.92
NaOH	-290.38	-282.01	-8.37	-284.78	-293.15
NaCl	-146.13	-132.18	-13.95	-130.56	-144.51
H$_2$O	-325.67	-327.18	1.51	-335.16	-333.65
OH$^-$	-310.78	-305.94	-4.84	-315.44	-320.28

Table S6 Energies (kcal·mol^{-1})

	a	b	c	d
1 + 2 NaOCl + 3 NaOH → 5 NaCl + H$_2$O + **3** + OH$^-$	-22.77	-92.52	-91.24	-79.08
1 + 2 NaOCl + 3 NaOH → 5 NaCl + H$_2$O + **3a** + OH$^-$	-18.31	-88.06	-86.78	-74.62

a: considering NaCl as having no vibrational frequencies.
b: considering NaCl as having one vibrational frequency (i.e. as covalently bonded).
c: considering NaOCl, NaOH and NaCl as having only covalent bond between O-H and O-Cl.
d: considering NaOCl, NaOH and NaCl without correction of Gibbs free energy.

5.6 References

1 (a) Costas, M.; Mehn, M. P.; Jensen, M. P.; Que, L., Jr. *Chem. Rev*. **2004**, *104*, 939–986, (b) Solomon, E. I.; Brunold, T. C.; Davis, M. I.; Kemsley, J. N.; Lee, S.-K.; Lehnert, N.; Neese, F.; Skulan, A. J.; Yang, Y.-S.; Zhou, *J. Chem. Rev*., **2000**, *100*, 235-350, (c) Punniyamurthy, T.; Velusamy, S.; Iqbal, J. Chem. Rev. **2005**, *105*, 2329–2363.

2 (a) Decker, A.; Solomon, E. I. *Curr. Opin. Chem. Biol*. **2005**, *9*, 152–163. (b) Bertini, I.; Gray, H. B.; Stiefel, E. I.; Valentine, J. S. Biological.Inorganic Chemistry. Structure & Reactivity; University Science Books: Sausalito, CA, **2007**. (c) Meunier, B. *Chem. Rev*. **1992**, *92*, 1411–1456. (d) Nam, W. *Acc. Chem. Res*. **2015**, *48*, 2415–2423. (e) Oloo, W. N.; Que, L. *Acc. Chem. Res.* **2015**, *48*, 2612–2621.

3 Shearer, J. *Acc. Chem. Res*. **2014**, *47*, 2332–2341.

4 (a) Cho, J.; Kang, Y.; Liu, L. V; Sarangi, R.; Solomon, E. I.; Nam, W. *Chem. Sci*. **2013**, *4*, 1502–1508. (b) Honda, K.; Cho, J.; Matsumoto, T.; Roh, J.; Furutachi, H.; Tosha, T.; Kubo, M.; Fujinami, S.; Ogura, T.; Kitagawa, T.; Suzuki, M. *Angew. Chem. Int. Ed*. **2009**, *48*, 3304–3307.

5 (a) Corona, T.; Pfaff, F. F.; Acua-Pares, F.; Draksharapu, A.; Whiteoak, C. J.; Martin-Diaconescu, V.; Lloret-Fillol, J.; Browne, W. R.; Ray, K.; Company, A. *Chem. - Eur. J.* **2015**, *21*, 15029–15038. (b) Pfaff, F. F.; Heims, F.; Kundu, S.; Mebs, S.; Ray, K. *Chem. Commun*. **2012**, *48*, 3730–3732.

6 (a) Draksharapu, A.; Codolà, Z.; Gómez, L.; Lloret-Fillol, J.; Browne, W. R.; Costas, M. *Inorg. Chem*. **2015**, *54*, 10656–10666. (b) Pirovano, P.; Farquhar, E. R.; Swart, M.; McDonald, A. R. *J. Am. Chem. Soc.* **2016**, *138*, 14362–14370. (c) Corona, T.; Draksharapu, A.; Padamati, S. K.; Gamba, I.; Martin-Diaconescu, V.; Acuña-Parés, F.; Browne, W. R.; Company, A. *J. Am. Chem. Soc.* **2016**, *138*, 12987-12996.

7 Corona, T.; Company, A. *Chem. - Eur. J.* **2016**, *22*, 13422–13429.

8 (a) Camasso, N. M.; Sanford, M. S. *Science* **2015**, *347*, 1–7. (b) Riordan, C. G. *Science* **2015**, *347*, 1203.

9 (a) Gray, H. B.; Hare, C. R. *Inorg. Chem*. **1962**, *1*, 363–368. (b) O'Halloran, K. P.; Zhao, C.; Ando, N. S.; Schultz, A. J.; Koetzle,T. F.; Piccoli, P. M. B.; Hedman, B.; Hodgson, K. O.; Bobyr, E.; Kirk, M. L.; Knottenbelt, S.; Depperman, E. C.; Stein, B.; Anderson, T. M.;Cao, R.; Geletii, Y. V.; Hardcastle, K. I.; Musaev, D. G.; Neiwert, W.A.; Fang, X.; Morokuma, K.; Wu, S.; Kögerler, P.; Hill, C. L. *Inorg. Chem.* **2012**, *51*, 7025–7031.

10 Wieghardt, K.; Schmidt, W.; Herrmann, W.; Kueppers, H. J. *Inorg. Chem*. **1983**, *22*, 2953–2956.

11 Bossek, U; Nühlen, D.; Bill, E.; Glaser, T.; Krebs, C.; Weyhermüller, T.; Wieghardt, K.; Lengen, M.; Trautwein, A.X. *Inorg. Chem*. **1997**, *36*, 2834-2843.

12 (a) Swart, M. *Chem. Phys. Lett*. **2013**, *580*, 166-171. (b) Becke, A. D. *Phys. Rev. A* **1988**, *38*, 3098-3100. (c) Perdew, J. P. *Phys. Rev. B* **1986**, *33*, 8822-8824.

13 At S12g/TZ2P//BP86-D3/TDZP

14 (a) Klamt, A.; Schüürmann, G. *J. Chem. Soc. Perkin Trans.* 2, **1993**, 799-805. (b) Pye, C. C.; Ziegler, T. *Theor. Chem. Acc*. **1999**, *101*, 396-408. (c) Swart, M.; Rösler, E.; Bickelhaupt, F. M. *Eur. J. Inorg. Chem.* **2007**, 3646-3654.

15 van Lenthe, E.; Baerends E. J.; Snijders, J. G. *J. Chem. Phys*. **1993**, *99*, 4597-4610

16 Tak, H.; Lee, H.; Kang, J.; Cho, J. *Inorg. Chem. Front*. **2016**, *3*, 157–163.

17 In the absence of Ni(II) or **1**, NaOCl is stable in CH3CN.

18 (a) Hage, R.; Krijnen, B.; Warnaar, J. B.; Hartl, F.; Stufkens, D. J.; Snoeck, T. L. *Inorg. Chem*. **1995**, *34*, 4973–4978. (b) Angelone, D.; Abdolahzadeh, S.; de Boer, J. W.; Browne, W. R. *Eur. J. Inorg. Chem.*, **2015**, *21*, 3532–3542.

19 Mandimutsira, B. S.; Yamarik, J. L.; Brunold, T. C.; Gu, W.; Cramer, S. P.; Riordan, C. G. *J. Am. Chem. Soc.* **2001**, *123*, 9194–9195, PhTttBu = Phenyltris((tert-butylthio)methyl)borate.

20 Itoh, S.; Bandoh, H.; Nakagawa, M.; Nagatomo, S.; Kitagawa, T.; Karlin, K.D.; Fukuzumi, S. *J. Am. Chem. Soc.* **2001**, *123*, 11168–11178.

21 Kieber-Emmons, M. T.; Schenker, R.; Yap, G. P. A.; Brunold, T. C.; Riordan, C. G. *Angew. Chem., Int. Ed*. **2004**, *116*, 6884–6886, tmc = 1,4,8,11-tetramethyl-1,4,8,11-tetraazadodecane.

22 Rettenmeier, C. A.; Wadepohl, H.; Gade, L. H. *Angew. Chem. Int. Ed.* **2015**, *54*, 4880–4884, iso-pmbox = bis(oxazolinylmethylidene)pyrrolidine.

23 Nash, T., *Biochem. J.* **1953**, *55*, 416-421.

24 Baerends, E. J.; Ziegler, T.; Autschbach, J.; Bashford, D.; Berger, A.; Bérces, A; Bickelhaupt, F. M.; Bo, C.; de Boeij, P. L.; Boerrigter, P. M.; Borini, S.; Bulo, R. E.; Cavallo, L.; Chong, D. P.; Deng, L.; Dickson, R. M.; van Duin, A. C. T.; Ellis, D. E.; Faassen, M. V.; Fan, L.; Fischer, T. H.; Fonseca Guerra, C.; Ghysels, A.; Giammona, A.; van Gisbergen, S. J. A.; Götz, A. W.; Groeneveld, J. A.; Gritsenko, O. V.; Grüning, M.; Gusarov, S.; Harris, F. E.; Heine, T.; van den Hoek, P.; Jacob, C. R.; Jacobsen, H.; Jensen, L.; Kadantsev, E. S.; Kaminski, J. W.; van Kessel, G.; Klooster, R.; Kootstra, F.; Kovalenko, A.; Krykunov, M. V.; van Lenthe, E.; Louwen, J. N.; McCormack, D. A.; McGarrity, E.; Michalak, A.; Mitoraj, M.; Neugebauer, J.; Nicu, V. P.; Noodleman, L.; Osinga, V. P.; Patchkovskii, S.; Philipsen, P. H. T.; Post, D.; Pye, C. C.; Ravenek, W.; Rodríguez, J. I.; Romaniello, P.; Ros, P.; Schipper, P. R. T.; Schreckenbach, G.; Seldenthuis, J. S.; Seth, M.; Skachkov, D. G.; Snijders, J. G.; Solà, M.; Swart, M.; Swerhone, D.; te Velde, G.; Vernooijs, P.; Versluis, L.; Visscher, L.; Visser, O.; Wang, F.; Wesolowski, T. A.; van Wezenbeek, E. M.; Wiesenekker, G.; Wolff, S. K.; Woo, T. K.; Yakovlev, A. L. *ADF2012.01*, (**2012**) SCM, Amsterdam

25 te Velde, G.; Bickelhaupt, F. M.; Baerends, E. J.; Fonseca Guerra, C.; van Gisbergen, S. J. A.; Snijders J. G.; Ziegler, T. *J. Comput. Chem.*, **2001**, *22*, 931-967.

26 Swart, M.; Bickelhaupt, F. M. *J. Comput. Chem.*, **2008**, *29*, 724-734.

27 Chong, D. P.; van Lenthe, E.; van Gisbergen S. J. A.; Baerends, E. J. *J. Comput. Chem.*, **2004**, *25*, 1030-1036.

28 van Lenthe, E.; Baerends, E. J. *J. Comput. Chem.*, **2003**, *24*, 1142-1156.

29 Wolff, S. K. *Int. J. Quantum Chem.*, **2005**, *104*, 645-659.

30 Becke, A. D. *Phys. Rev. A*, **1988**, *38*, 3098-3100.

31 Grimme, S.; Antony, J.; Ehrlich S.; Krieg, H. *J. Chem. Phys.*, **2010**, *132*, 154104.

32 Klamt, A.; Schüürmann, G. *J. Chem. Soc. Perkin Trans. 2*, **1993**, 799-805.

33 Swart, M.; Rösler E.; Bickelhaupt, F. M. *Eur. J. Inorg. Chem.*, **2007**, 3646-3654.

34 Becke, A. *J. Chem. Phys.*, **1988**, *88*, 2547-2553.

35 Franchini, M.; Philipsen, P. H. T.; Visscher, L. *J. Comput. Chem.*, **2013**, *34*, 1819-1827.

36 Swart, M. *Chem. Commun.*, **2013**, *49*, 6650-6652.

37 Schipper, P. R. T.; Gritsenko, O. V.; van Gisbergen, S. J. A.; Baerends, E. J. *J. Chem. Phys.* **2000**, *112*, 1344-1352.

38 Hopmann, K. H.; Pelmenschikov, V.; Du, W.-G. H.; Noodleman, L. in *Spin States in Biochemistry and Inorganic Chemistry: Influence on Structure and Reactivity*, eds. M. Swart and M. Costas, John Wiley & Sons, Chichester, UK, 2016, pp. 297-325.